

# Revisiting the Relationship between Eyewall Contraction and Intensification

DANIEL P. STERN AND JONATHAN L. VIGH

*National Center for Atmospheric Research,\* Boulder, Colorado*

DAVID S. NOLAN

*Rosenstiel School of Marine and Atmospheric Science, University of Miami, Miami, Florida*

FUQING ZHANG

*The Pennsylvania State University, University Park, Pennsylvania*

(Manuscript received 11 September 2014, in final form 25 November 2014)

## ABSTRACT

In the widely accepted convective ring model of tropical cyclone intensification, the intensification of the maximum winds and the contraction of the radius of maximum winds (RMW) occur simultaneously. This study shows that in idealized numerical simulations, contraction and intensification commence at the same time, but that contraction ceases long before peak intensity is achieved. The rate of contraction decreases with increasing initial size, while the rate of intensification does not vary systematically with initial size. Utilizing a diagnostic expression for the rate of contraction, it is shown that contraction is halted in association with a rapid increase in the sharpness of the tangential wind profile near the RMW and is not due to changes in the radial gradient of the tangential wind tendency. It is shown that a number of real storms exhibit a relationship between contraction and intensification that is similar to what is seen in the idealized simulations. In particular, the statistical distribution of intensifying tropical cyclones indicates that, for major hurricanes, most contraction is completed prior to most intensification.

By forcing a linearized vortex model with the diabatic heating and frictional tendencies from a simulation, it is possible to qualitatively reproduce the simulated secondary circulation and separately examine the vortex responses to heating and friction. It is shown that heating and friction both contribute substantially to boundary layer inflow. They also both contribute to the contraction of the RMW, as the positive wind tendency from heating-induced inflow is maximized inside of the RMW, while the net negative wind tendency from friction and frictionally induced inflow is maximized outside of the RMW.

## 1. Introduction

The convective ring model of tropical cyclone intensification (Shapiro and Willoughby 1982, hereafter SW82; Willoughby et al. 1982, hereafter W82; Willoughby 1990) implies generally that the intensification of the maximum winds and the

contraction of the radius of maximum winds (RMW) occur simultaneously. In this paradigm, the secondary circulation induced by eyewall heating leads to both contraction and “spinup” through radial advection of absolute angular momentum  $M$ . Herein, we show that in idealized numerical simulations of tropical cyclones, most contraction occurs prior to most intensification. We use flight-level observations to show that this process is also apparent in real tropical cyclones. For the simulations, a kinematic analysis shows that a rapid increase in the sharpness of the wind field is responsible for the rapid slowing of contraction. Finally, we use a linear vortex model to further investigate the dynamics of intensification and contraction.

---

\*The National Center for Atmospheric Research is sponsored by the National Science Foundation.

---

Corresponding author address: Daniel P. Stern, National Center for Atmospheric Research, 3450 Mitchell Lane, Boulder, CO 80301.  
E-mail: dstern@ucar.edu

SW82 used the balanced vortex model of Eliassen (1951) to solve for the secondary circulation (radial and vertical flow) induced by heating in idealized hurricane-like vortices.<sup>1</sup> From this, they calculated the tendency in the primary circulation (tangential wind  $v$ ) associated with the advection of angular momentum by the secondary circulation. There exists an analytical solution for barotropic vortices with constant stratification, and SW82 found that for a point heat source located just inside of the RMW, the tendency of  $v$  is maximized at the RMW. SW82 also presented numerical solutions to the Sawyer–Eliassen equation for both barotropic and more realistic baroclinic vortices and found that, in almost all cases, heating at the RMW yields a  $v$  tendency that is maximized inward of the RMW. They stated that this is because all the vortices used in the numerical calculations had smooth radial profiles of  $v$ , such that vorticity was always maximized inward of the RMW. They found that except when the radial wind  $u$  has a sharp peak at the RMW, the maximum in  $v$  tendency will be inward of the RMW, and so “the RMW tends to move inward as the vortex intensifies.” They concluded, “In the absence of other physical processes, the radial profile of  $v$  would develop a sharp peak near the maximum of  $dv/dt$ . The continued inward movement of the RMW depends on processes that maintain both the heat and momentum sources and the rounded profile of  $v$  near the RMW.” In a similar theoretical study to SW82, Schubert and Hack (1982) used the Sawyer–Eliassen equation to show that the efficiency with which eyewall heating leads to the intensification of the vortex increases strongly with intensity itself. Schubert and Hack (1982) also qualitatively discussed contraction, stating that “one can picture the tendency for the radius of maximum wind to move inward until it coincides with the inner edge of the heated region.”

W82 presented observations from flights into tropical cyclones that are consistent with the model proposed by SW82 and coined the term “convective ring model” for the proposed mechanism by which tropical cyclones intensify and contract. Using multiple flight legs over the course of a flight to calculate tendencies of tangential wind, W82 found that during intensification, the  $v$  tendency was maximized inward of the RMW, implying contraction. W82 also showed time series of maximum wind and the RMW, with the RMW often contracting during intensification. Referring to convective rings, they write, “If the ring contains active convective heating, the most rapid increase in wind speed lies on the

inside of the wind maximum. The maximum will thus contract as it intensifies. This, rather than a general increase in wind speed, appears to be the means by which symmetric hurricanes intensify.” In a similar study using a much larger dataset Willoughby (1990) provided further evidence in favor of the convective ring model and stated, “Extensive observations show that convectively driven contracting maxima of the swirling wind constitute the primary mechanism for the intensification of hurricanes.”

An implicit conclusion of the above studies is that tropical cyclone intensification is generally coincident with contraction of the RMW and that one necessarily implies the other.<sup>2</sup> Although SW82 and W82 were themselves cautious in their explicit conclusions, this idea has since become widely accepted (Jorgensen 1984b; Holland 1997; Black et al. 2002; Kimball and Mulekar 2004; Kossin et al. 2007; Evans and Hart 2008; Pu et al. 2009; Houze 2010; Emanuel 2012; Chen et al. 2011; Judt and Chen 2013; Hogsett and Stewart 2014). An example of a study that follows this paradigm is Kimball and Mulekar (2004), who presented an observational climatology of tropical cyclone size, using the extended best-track (EBT) dataset. Throughout, it is assumed that contraction and intensification are simultaneous and that intensifying storms are therefore contracting storms. For example, the fact that they find more weakening storms than intensifying storms with “small” RMWs is taken as evidence that the weakening storms “have completed the eyewall contraction process and are now ready to decay.” As we will discuss later, several figures in Kimball and Mulekar actually are consistent with the idea that contraction ceases prior to most intensification.

In section 2 of this study, we will present evidence from idealized numerical simulations that indicates that while contracting storms are indeed generally intensifying, intensifying storms are not necessarily contracting. The belief that these different processes happen simultaneously stems, in part, from the conception (by some authors) of the RMW as a material surface that can be advected, and that contracts while conserving angular momentum. We will show that this is not true. We derive a diagnostic expression for the rate of contraction of the RMW and use it to show that, in our simulations, the “sharpening” of the wind field around the RMW is the reason that contraction reaches

---

<sup>1</sup> There were other similar studies undertaken around this time, and SW82 were inspired in part by Smith (1981), who examined the effect of mass removal (as a proxy for diabatic heating) on the secondary circulation in simplified one- and three-layer models.

---

<sup>2</sup> Note that SW82 and W82 do not explicitly make this claim, and based on other context within their studies as well as some of their own figures, it appears that they recognized that intensification does not necessarily imply contraction.

completion long before rapid intensification (RI) does. In section 3, we present observations of contraction from a number of storms that are consistent with our idealized simulations. In section 4, we investigate the dynamical mechanisms by which contraction and intensification occur, using a linear vortex model. We will show that eyewall heating is largely responsible for both the intensification of the inner core and the contraction of the RMW. In contrast to the conclusions of several recent studies, friction has a net negative contribution to intensification, though it does act to contract the RMW. In section 5, we provide a summary of our results as well as a discussion in the context of previous studies.

## 2. Idealized WRF simulations

### a. Model setup and overview of contraction and intensification

We use WRF, version 3.1.1, to simulate idealized tropical cyclones on a doubly periodic  $f$  plane, in a homogeneous environment characterized by the moist-tropical sounding of Dunion (2011), with a uniform SST of 28°C. The storms are embedded within a uniform 5 m s<sup>-1</sup> easterly flow, and there is no vertical wind shear. All simulations use 40 vertical half-levels and utilize a triply nested grid with grid spacings of 18, 6, and 2 km and domain sizes of 4320 km × 4320 km, 720 km × 720 km, and 360 km × 360 km, respectively. We use the WSM6 microphysics parameterization and the Yonsei University (YSU) boundary layer parameterization. No parameterizations of radiation or convection are utilized. Further details can be found in Stern and Nolan (2011, hereafter SN11), who examined these same simulations.

The initial condition in each simulation is a modified Rankine vortex with maximum winds of 25 m s<sup>-1</sup> at 1500-m height, where the radial profile of tangential wind is given by

$$v = \begin{cases} v_{\max} \left( \frac{r}{r_{\max}} \right), & r \leq r_{\max} \\ v_{\max} \left( \frac{r_{\max}}{r} \right)^a, & r > r_{\max} \end{cases} \quad (1)$$

Here,  $v_{\max}$  and  $r_{\max}$  are the initial maximum winds and initial RMW, respectively. The simulations differ in either the initial RMW (36, 90, 180 km) or in the radial decay parameter  $a$  (0.25, 0.50, 0.75, 1.00). Figure 1 shows the initial radial profiles of tangential wind at the lowest model level for all simulations (on the 18-km domain). Simulations are named as in, for example, R90A50, where the number following “R” is the initial RMW in kilometers and the number following “A” is the initial decay parameter multiplied by 100. The seven simulations

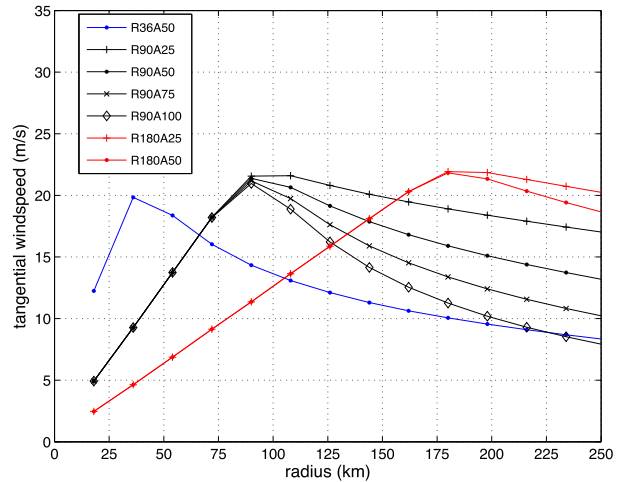


FIG. 1. Initial radial profile of tangential wind for each simulation, on the outer (18 km) grid. Each simulation is labeled by its initial RMW (the number following “R”) and its initial Rankine decay coefficient (the number following “A,” divided by 100).

are listed in Table 1. As can be seen in Fig. 1,  $a = 0.25$  gives the slowest decay of  $v$  with radius and  $a = 1.0$  (which defines a Rankine vortex) gives the fastest. SN11 designed these simulations with the goal of obtaining quasi-steady-state hurricanes of different sizes. Time series of the maximum surface (10 m) wind speed and of the RMW at the lowest model level are shown in Figs. 2a and 2b, respectively (this is similar to Fig. 13 of SN11). Figures 2c and 2d are similar to Figs. 2a and 2b but normalize the wind speed by its lifetime maximum and the RMW by its initial size, respectively. After some period of time, all simulations achieve a quasi-steady-state size. This quasi-steady-state size of the RMW increases with increasing initial size (e.g., the R180 simulations are the largest, R36 the smallest) and with decreasing  $a$  (e.g., the A25 simulations are the largest, A100 are the smallest). On the other hand, there is no apparent systematic relationship between either initial RMW or  $a$  and the quasi-steady-state intensity achieved, which varies from 60 to 80 m s<sup>-1</sup> (corresponding to category 4 and 5 hurricanes).

As seen in Fig. 2b, the time to achieve a quasi-steady size increases with initial RMW. On the other hand, there is no systematic dependency of the time to achieve quasi-steady intensity on the initial size (Fig. 2a). Contraction begins at about  $t = 12$  h in all simulations. R36A50 achieves a quasi-steady-state size the quickest, by  $t = 24$  h, while the R180 simulations take the longest, not reaching quasi-steady-state size until  $t = 108$ – $120$  h. Quasi-steady-state intensity occurs by  $t = 96$ – $120$  h in all simulations. Therefore, the lag between the time to quasi-steady size and the time to quasi-steady intensity decreases with increasing initial size. For R36 and all

TABLE 1. List of simulations.

Simulation name	Initial RMW (km)	Rankine decay coefficient
R36A50	36	0.50
R90A25	90	0.25
R90A50	90	0.50
R90A75	90	0.75
R90A100	90	1.00
R180A25	180	0.25
R180A50	180	0.50

R90 simulations, the contraction of the RMW is complete long before a quasi-steady intensity is reached. Even though the period of contraction is much longer in the R180 simulations, most contraction still occurs prior

to most of the intensification. This was remarked upon briefly in SN11, and they noted, “This phenomenon is in contrast to what is generally believed to happen: that spinup occurs simultaneously with contraction, with the RMW ‘conserving’ its angular momentum.” SN11 also noted that contraction largely preceding intensification can be seen in the figures of a number of prior simulation studies (Willoughby et al. 1984; Kimball and Dougherty 2006; Wang 2008; Van Sang et al. 2008; Hill and Lackmann 2009) but that none of these studies (nor apparently any other such studies) had noted this behavior.

As noted in SN11, despite starting 5 times as large, the RMW of R180A50 is only twice as large as that of R36A50 at their respective quasi-steady-state sizes. This phenomenon can be seen in Fig. 2d, as the net fractional

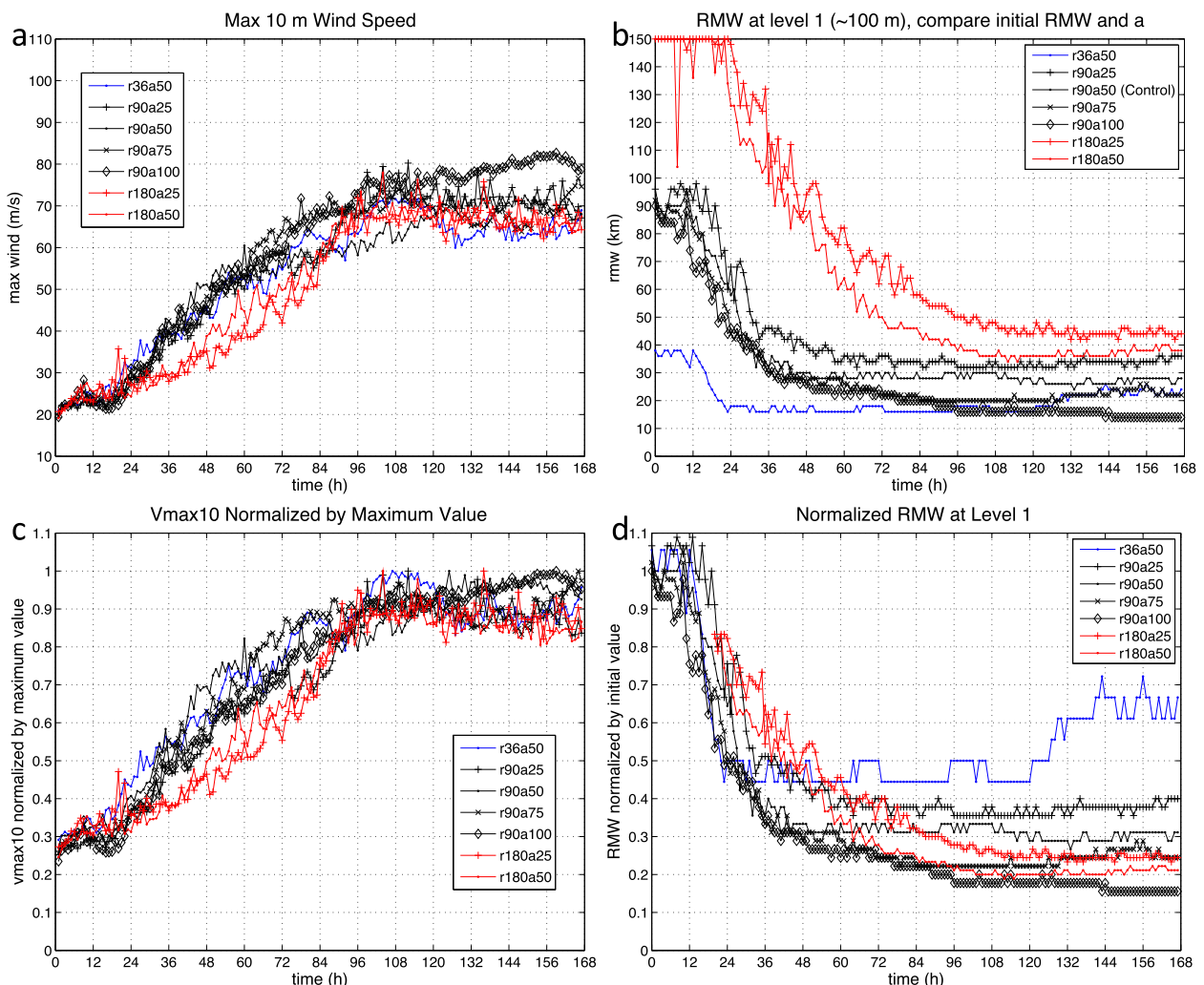


FIG. 2. Time series of (a) the maximum 10-m wind speed, (b) the RMW at the lowest model level, (c) the maximum 10-m wind speed normalized by the lifetime maximum, and (d) the RMW at the lowest model level normalized by the initial value. Note that owing to the size of the domain examined (inside of 150-km radius), the RMW for the R180 simulations is not shown to exceed 150 km in (b), and the normalized RMW is not plotted in (d) prior to the time at which the RMW is less than 150 km.

contraction at quasi-steady state increases with increasing initial RMW. The quasi-steady RMW is roughly 45%, 35%, and 20% of the initial RMW for R36A50, R90A50, and R180A50, respectively.

Independent of SN11, Vigh (2010) found observationally that contraction tends to slow down or cease around the time of eye formation. Since Vigh (2010) also found that eye formation occurs on average at an intensity of only 58 knots (kt;  $1 \text{ kt} = 0.51 \text{ m s}^{-1}$ ), this implies that many storms continue to intensify well beyond the time when the contraction of the RMW has ceased. Vigh (2010) wrote, “The greatest contraction in  $r_{\text{max}}$  occurs in the day or so before eye formation. During the subsequent intensification,  $r_{\text{max}}$  does not contract much more than the  $r_{\text{max}}$  achieved at the time the eye forms.” The rest of this study will further investigate this phenomenon that was identified in the simulations of SN11 and the observations of Vigh (2010).

*b. Does the RMW contract while maintaining constant absolute angular momentum?*

It is sometimes assumed that the RMW contracts as if it were a material surface (Holland and Merrill 1984; Pu et al. 2009; Kieu 2012; Judt and Chen 2013), maintaining a constant value of  $M$ . For example, Emanuel (2012) explicitly makes the assumption that  $M$  is constant in time at the RMW in his derivation of an analytical expression for the time rate of change of the maximum wind speed for a slantwise moist neutral vortex in thermal wind balance. This assumption underlies the belief that contraction and spinup occur simultaneously. To examine the validity of this assumption, time–radius Hovmöller plots of  $M$  (at 2-km height<sup>3</sup>) for each simulation are shown in Fig. 3. In each panel, the RMW is overlaid in white. It can be seen that in general,  $M$  at the RMW decreases (by roughly 30%–50% of the initial value) during the rapid contraction phase, as the RMW propagates inward more rapidly than the nearby  $M$  surfaces. As contraction slows,  $M$  at the RMW begins to increase (as  $M$  surfaces are advected past the RMW), and intensification “in place” occurs. That most intensification occurs after contraction has slowed or halted can further be seen in Hovmöller plots of azimuthal-mean tangential wind speed (Fig. 4). If it were true that the RMW maintains its initial value of  $M$  throughout the intensification process, then contraction would indeed have a one-to-one relation with intensification. At least in our simulations, this is not the

case. And while it can be intuitive to think of the RMW as an  $M$  surface that is simply advected by the mean secondary circulation, there actually is no theoretical reason for this to be so. Even though at any given time,  $M$  is close to constant with height along the RMW (Stern and Nolan 2009; SN11), the RMW is not a material surface. Rather, the RMW is simply the location of a maximum in a field and need not obey conservation laws. It is not correct to think of the RMW as being advected. In the following section, we will derive a diagnostic expression for the contraction rate of the RMW, and this will help to explain the physical mechanisms of contraction.

*c. A kinematic understanding of contraction*

If the wind tendency is maximized inward of the RMW, then the RMW will generally contract. However, the rate of contraction depends critically on both the radial gradient of the wind tendency and the degree to which the radial profile of tangential wind is “peaked.” A local, diagnostic expression for the instantaneous rate of change of the RMW can be derived as follows. First, define the tangential wind  $V$  as a function of radius  $r$  and time  $t$ :

$$V = V(r, t). \quad (2)$$

At the RMW, the radial gradient of  $V$  is zero by definition:

$$\frac{\partial V[\text{RMW}(t), t]}{\partial r} = 0. \quad (3)$$

Note that (3) is only true when evaluated locally (in space and time) at the RMW (the location of which varies in time). Therefore, higher-order partial derivatives of (3) are not necessarily zero themselves. Next, take the total derivative of (3) with respect to time:<sup>4</sup>

$$\frac{d}{dt} \left\{ \frac{\partial V[\text{RMW}(t), t]}{\partial r} \right\} = 0, \quad (4)$$

and after applying the chain rule,

$$\frac{\partial}{\partial t} \left\{ \frac{\partial V[\text{RMW}(t), t]}{\partial r} \right\} + \frac{d\text{RMW}(t)}{dt} \frac{\partial}{\partial r} \left\{ \frac{\partial V[\text{RMW}(t), t]}{\partial r} \right\} = 0. \quad (5)$$

We can rearrange (5) to get an expression for the time rate of change of the RMW:

<sup>3</sup> We show  $M$  at 2-km height because it is representative of the low-level flow, but above the boundary layer (where  $M$  is not conserved) and above the region of strongly unbalanced flow.

<sup>4</sup> Note that we are defining the total derivative with respect to the RMW (i.e., the derivative follows the RMW, rather than the flow itself).

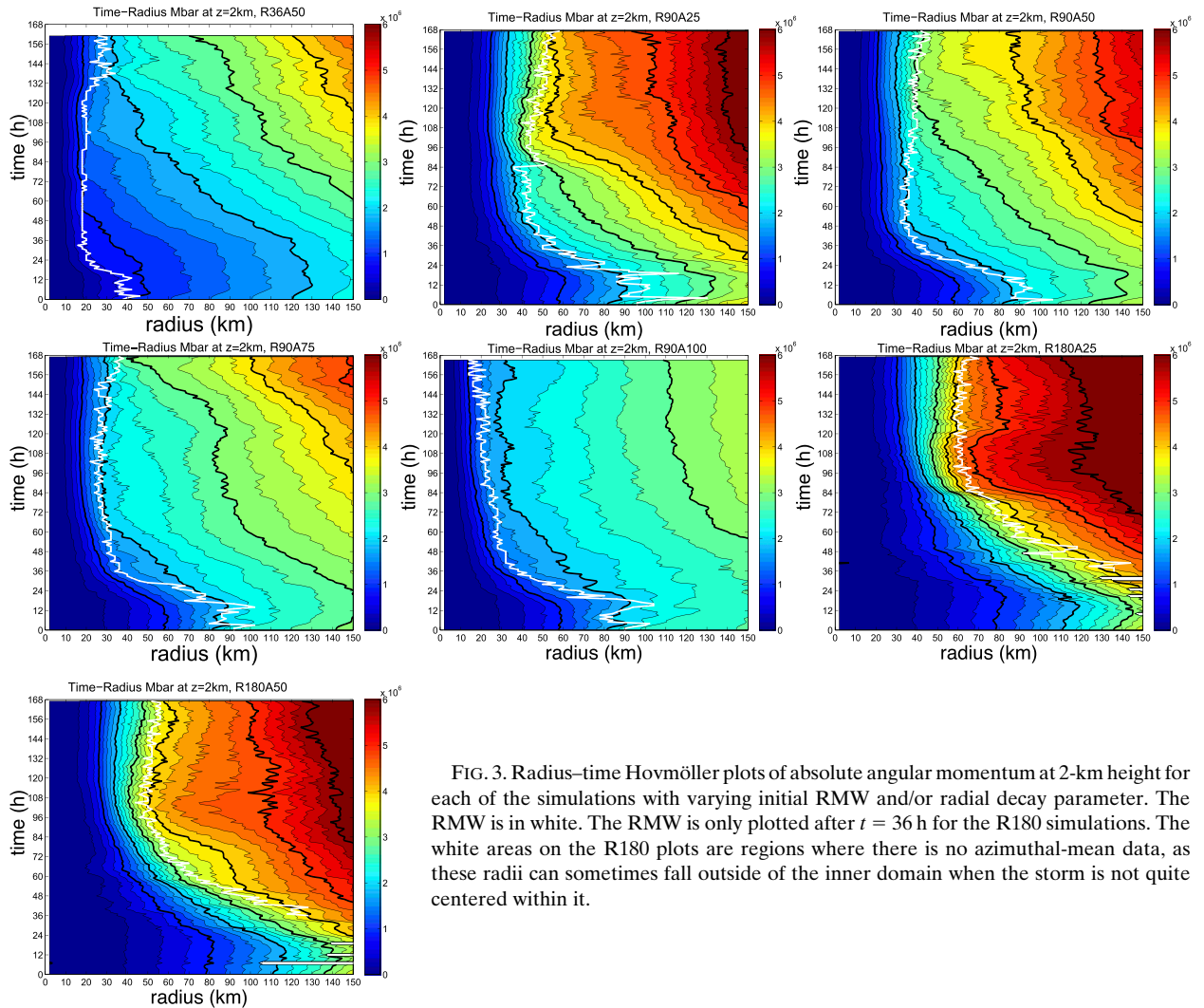


FIG. 3. Radius–time Hovmöller plots of absolute angular momentum at 2-km height for each of the simulations with varying initial RMW and/or radial decay parameter. The RMW is in white. The RMW is only plotted after  $t = 36$  h for the R180 simulations. The white areas on the R180 plots are regions where there is no azimuthal-mean data, as these radii can sometimes fall outside of the inner domain when the storm is not quite centered within it.

$$\frac{d\text{RMW}}{dt} = - \left. \frac{(\partial/\partial t)(\partial V/\partial r)}{\partial^2 V/\partial r^2} \right|_{\text{RMW}}. \quad (6)$$

Note that (6) is only valid when evaluated at the RMW. Finally, we can exchange the time and space partial derivatives in the numerator of (6):

$$\frac{d\text{RMW}}{dt} = - \left. \frac{(\partial/\partial r)(\partial V/\partial t)}{\partial^2 V/\partial r^2} \right|_{\text{RMW}}. \quad (7)$$

So from a kinematic perspective, the rate of contraction (or expansion) of the RMW depends on two properties: the radial gradient of the time tendency of  $V$  and the curvature or “sharpness” of the radial profile of  $V$ . Contraction will be slower when the radial gradient of the wind tendency is smaller, and contraction will also be slower when the wind profile is more peaked at the RMW. Note that W82 gave the following formula for the rate of contraction:

$$\frac{d\text{RMW}}{dt} = \frac{(\partial V/\partial t)_{\text{max}} - (\partial V/\partial t)_{\text{RMW}}}{\partial V/\partial r}, \quad (8)$$

where the term with the “max” subscript refers to the maximum wind tendency. It is apparent that (8) is essentially a finite-difference approximation to (7).

To better understand the contraction phenomenon in these simulations, we show in Fig. 5 the time–radius Hovmöller plots of  $(\partial/\partial r)(\partial V/\partial t)$  and  $\partial^2 V/\partial r^2$  for R90A50 (herein, the control simulation) at  $z = 250$  m.<sup>5</sup> Here,  $V$  is the azimuthal-mean tangential wind after applying a filter in time to remove scales less than 6 h (in order to reduce noise in derivatives). Also shown are the RMW from the

<sup>5</sup> We show this height because it is the lowest constant-height interpolated level (as described in SN11) and because the RMW at all heights is influenced by the RMW within the boundary layer (Stern and Nolan 2009; Stern et al. 2014).

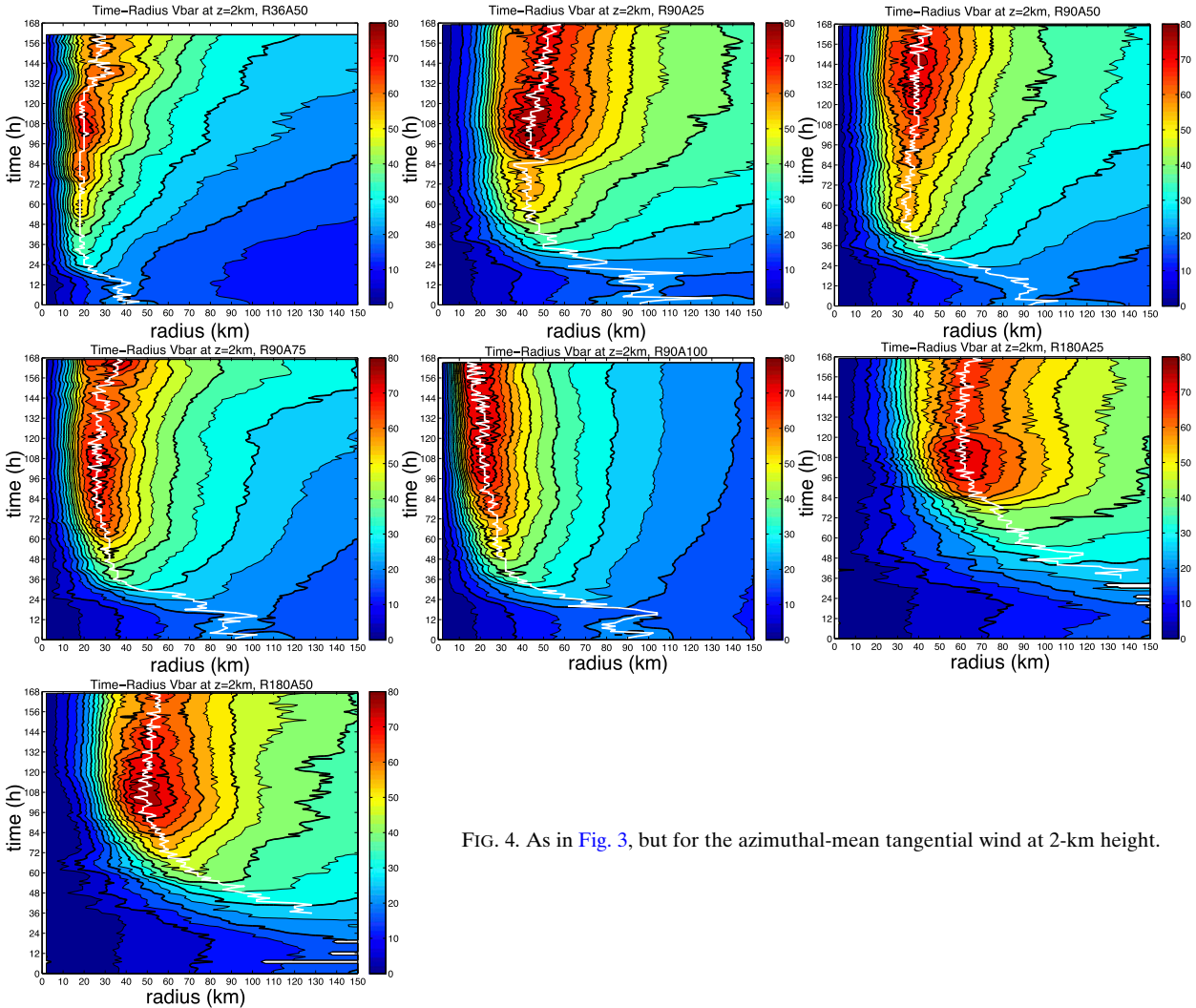


FIG. 4. As in Fig. 3, but for the azimuthal-mean tangential wind at 2-km height.

filtered winds and the filtered  $2.5 \text{ cm s}^{-1}$  azimuthal-mean vertical velocity. Note that although we use 6-min model output for calculating the filtered variables in Fig. 5, for clarity, we plot at 1-h intervals. In the control simulation, the contraction of the low-level RMW rapidly slows down around  $t = 36 \text{ h}$ . Note that  $\partial^2 V / \partial r^2$  is negative at and near the RMW at all times. The magnitude of this term increases around the time that contraction begins to slow down. The radial gradient of the  $V$  tendency is noisier, but it can be seen that around the RMW, it is negative during the period of contraction. Later on, there are alternating periods of negative and positive  $(\partial/\partial r)(\partial V/\partial t)$  at the RMW. Figures 6a and 6b show time series of  $(\partial/\partial r)(\partial V/\partial t)$  and of  $\partial^2 V/\partial r^2$  at the RMW at  $z = 250 \text{ m}$ . Shown in Fig. 6c is the diagnosed RMW tendency ( $\text{km h}^{-1}$ ) from (7) evaluated at the RMW. Finally, to verify the diagnosed tendency, Fig. 6d shows the rate of change of the RMW itself, from the filtered  $V$ , having

interpolated in radius (with a cubic spline) to 10-m grid spacing in order to obtain an RMW that more smoothly varies in time.<sup>6</sup> Contraction begins at around  $t = 12 \text{ h}$ , and accelerates for the next 12–18 h, reaching  $2\text{--}3 \text{ km h}^{-1}$  by  $t = 30 \text{ h}$ . Throughout this period,  $\partial^2 V/\partial r^2$  is nearly constant, while  $(\partial/\partial r)(\partial V/\partial t)$  increases in magnitude. Therefore, it is the increasing radial gradient

<sup>6</sup> Because the RMW itself changes discretely at our chosen grid spacing (2 km) for azimuthal averaging, the time series of the “actual” rate of change of RMW is mostly flat, punctuated by spikes at the few times when the RMW discretely jumps (not shown). Nevertheless, when averaged over the period of contraction, the diagnosed mean contraction rate is in excellent agreement with the actual mean contraction rate. Interpolating with splines to 10-m grid spacing yields a time series of RMW tendency that is in excellent agreement with the time series of diagnosed RMW tendency (Figs. 6c,d).

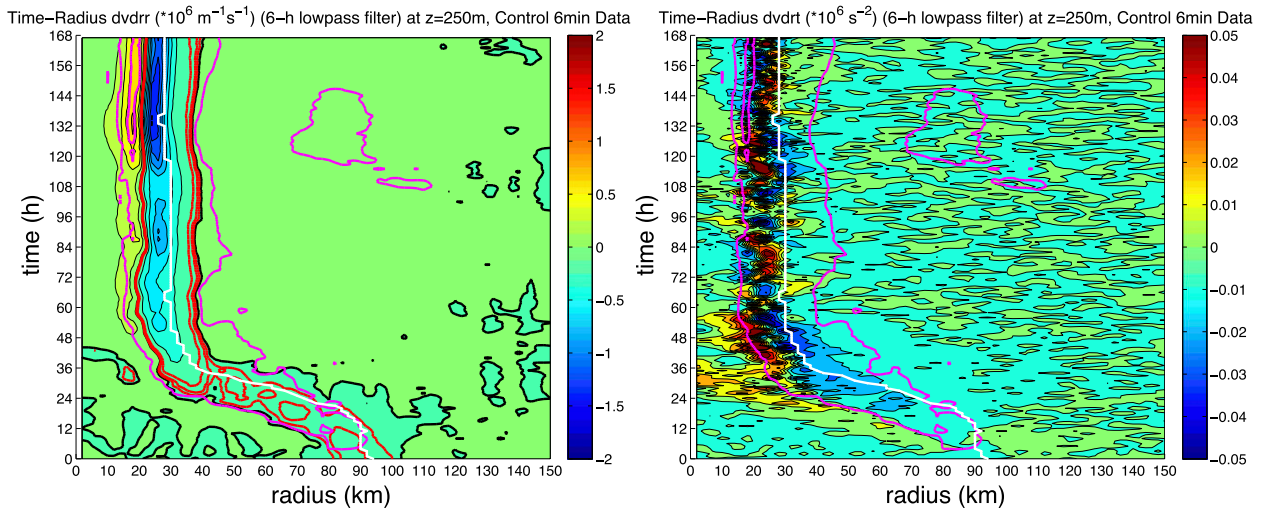


FIG. 5. Radius–time Hovmöller plots of (left)  $\partial^2 V / \partial r^2$  and (right)  $(\partial/\partial r)(\partial V/\partial t)$ , at  $z = 250\text{-m}$  height in the control simulation, using data at 6-min output frequency. The tangential wind field was filtered in time to remove scales less than 6 h. The RMW from the filtered wind is plotted in white, and the  $2.5 \text{ cm s}^{-1}$  updraft from the filtered vertical velocity is contoured in magenta. In (left), the zero contour of  $\partial^2 V / \partial r^2$  is in black, and the  $-0.01$ ,  $-0.02$ , and  $-0.05$  contours are in red.

of the  $V$  tendency that causes the increasing rate of contraction prior to and during the beginning of RI.

The rate of contraction of the RMW in the control simulation rapidly slows down at around  $t = 36$  h. Since the earlier acceleration of contraction is due to an increasing radial gradient of the  $V$  tendency, one might guess that the slowdown is associated with an analogous decrease in this gradient. This is not the case, however, as  $(\partial/\partial r)(\partial V/\partial t)$  actually continues to increase in magnitude through  $t = 48$  h, which, all else being equal, would lead to a continued acceleration of the contraction. Instead, the slowing of contraction and its eventual halt is associated with a rapid sharpening of the RMW, with a tenfold increase in the magnitude of  $\partial^2 V / \partial r^2$  over a 6-h period. Interestingly, it is apparent from the Hovmöller plots that the inward propagation of the inner edge of the eyewall updraft rapidly slows down about 12 h prior to the slowing of the RMW contraction.

The diagnosed RMW tendency is on average about zero beyond  $t = 48$  h, which is consistent with the fact that the RMW is nearly constant through the remainder of the simulation. While  $(\partial/\partial r)(\partial V/\partial t)$  decreases in magnitude from  $t = 48$  to 60 h and is near zero (on average) from  $t = 60$  to 84 h, there are periods ( $t = 108$ – $132$  h) where this term achieves the same magnitude as it had during the period of rapid contraction. There are other times when  $(\partial/\partial r)(\partial V/\partial t)$  is large and positive, such as  $t = 144$ – $156$  h. Yet there are neither substantial contractions nor expansions of the RMW after  $t = 48$  h. This is because  $\partial^2 V / \partial r^2$  continues to increase in magnitude until the end of the simulation, by which time this term has increased another 5 times. This sharpening of

the RMW can be further seen in Fig. 7, which shows radial profiles of the (unfiltered) azimuthal-mean tangential wind at the start of each day. Starting from a rather rounded profile near the initial RMW, the peak winds become much sharper from 0000 UTC day 2 to 0000 UTC day 3 and continue to sharpen thereafter, while the RMW remains nearly constant. Essentially, the ever-increasing sharpness of the RMW renders it more and more difficult for significant contraction or expansion to occur.

### 3. Observations of contraction

While it seems clear that there is a lag between contraction of the RMW and intensification in the above simulations, it is of course possible that tropical cyclones behave differently in nature. Here, we present observations that indicate that a similar relationship between contraction and intensification is seen in at least a substantial fraction of real TCs. From 1989 through 2012, 5611 aircraft penetrations have been made through the center of 382 tropical cyclones in the Atlantic basin. For each penetration, a vortex data message (VDM) is transmitted in real time, containing basic information on storm intensity and structure such as the storm position, minimum surface pressure, maximum flight-level winds, and the RMW. Vigh et al. (2012) assembled this dataset and used it to study the initial formation of the eye. Vigh (2010) found that a large number of observed storms exhibit behavior that is qualitatively similar to that of our simulations: rapid contraction near the start of intensification, followed by most intensification occurring

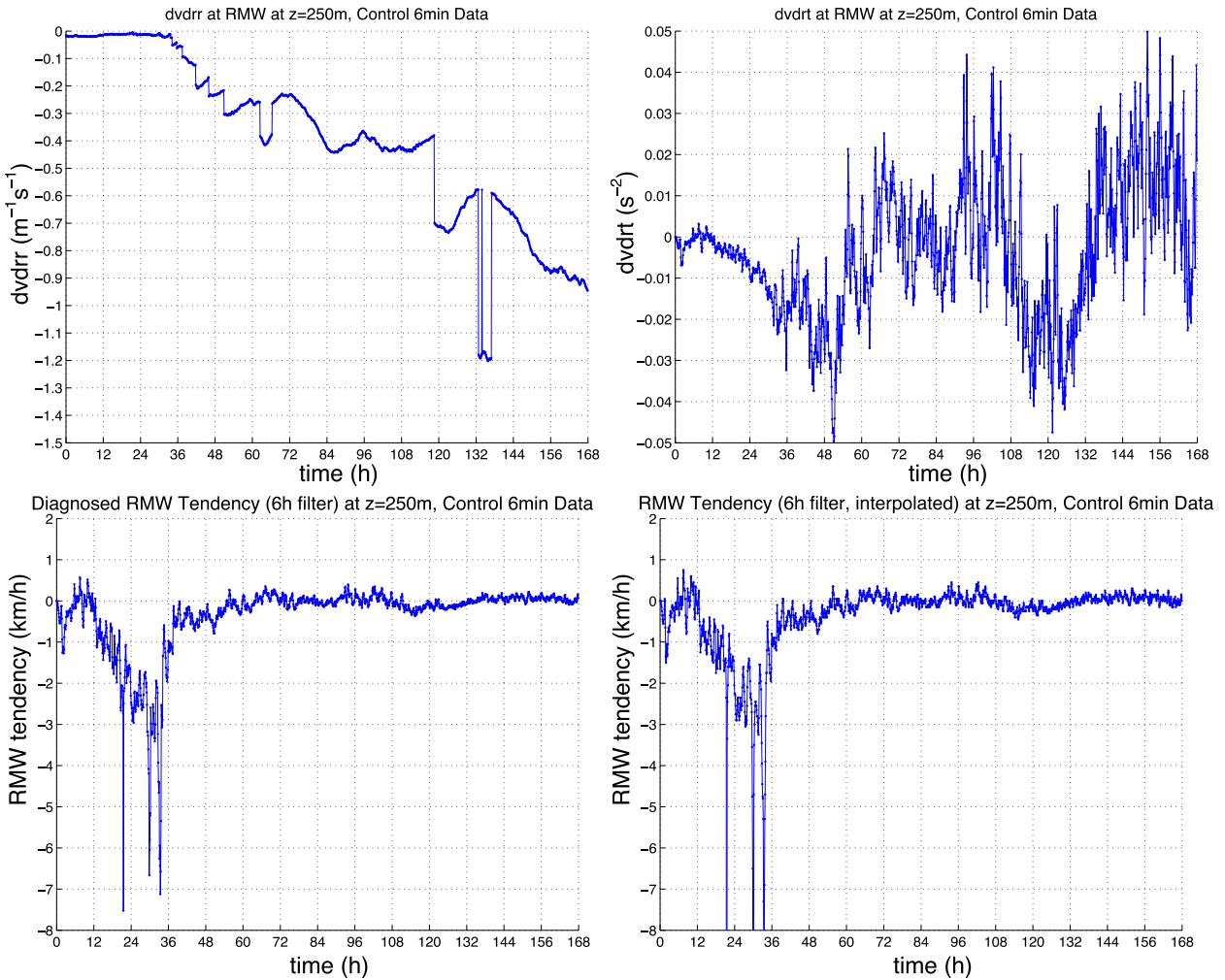


FIG. 6. Time series of (top left)  $\partial^2V/\partial r^2$ , (top right)  $(\partial/\partial r)(\partial V/\partial t)$ , (bottom left) the diagnosed time tendency of the RMW [from (7)], and (bottom right) the actual tendency of the RMW. Each time series is evaluated at the RMW at  $z = 250\text{-m}$  height in the control simulation (from 6-min data). Prior to the calculation of derivatives, the tangential wind field was filtered in time to remove scales less than 6 h. In (bottom right), the filtered tangential wind field was interpolated in radius from 2-km to 10-m grid spacing using cubic splines in order to calculate an RMW that varies more smoothly in time.

at a nearly steady RMW. Some examples of such observed storms are shown in Fig. 8 for Hurricanes Andrew (1992), Isidore (2002), Lili (2002), and Emily (2005). In each of these cases, the storm undergoes a period of intensification from tropical storm to major-hurricane strength (100 kt). And in each of these cases, although the period of contraction overlaps with the period of intensification, contraction is essentially complete by the time hurricane strength (65 kt) is achieved, long before peak intensity.

There are also some storms that appear to evolve in a manner more similar to that of the classical model, and two such examples are shown in Fig. 9: Opal (1995) and Mitch (1998). In both of these cases, the RMW seems to contract for a longer period of time, encompassing most of the period of RI.

It can be seen in both Figs. 8 and 9 that the RMW is a very noisy field and is difficult to estimate observationally. This is due both to observing techniques and to sampling. Until recently, the only actual measurement of the RMW was from flight-level winds; the surface RMW was estimated visually. Since the installation of the Stepped Frequency Microwave Radiometer (SFMR) on the NOAA P3s in 1998 (N42RF) and 2005 (N43RF) and on the Air Force C-130s beginning in 2007, the surface RMW has been more accurately determined. Nevertheless, much uncertainty remains, owing to limited sampling both in space and time. There can be a substantial stationary asymmetry to the RMW, which can easily lead to apparent time tendencies that are spurious. In addition, transient asymmetries of the RMW as well as uncertainties in the storm center location can further

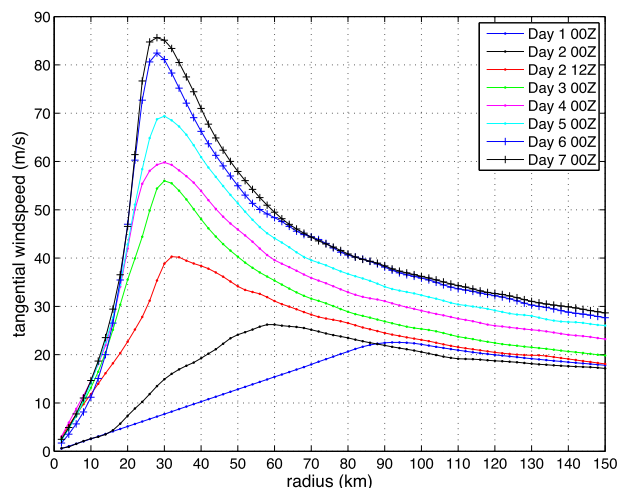


FIG. 7. Radial profiles of azimuthal-mean tangential wind for the control simulation, at 0000 UTC each day from day 1 to day 7. To illustrate the period of rapid contraction, 1200 UTC day 2 is also plotted.

increase the noise. Therefore, it is often difficult to accurately determine the time evolution of the RMW in observed storms. Nevertheless, based on the available data, it is clear that many storms do indeed exhibit a relationship between contraction and intensification that is similar to what is seen in our idealized simulations. The question remains as to why storms seem to contract in this manner.

We note that despite the fact that [Kimball and Mulekar \(2004\)](#) assume that contraction and intensification are simultaneous, their figures are actually consistent with our numerical results. Their Fig. 15 indicates that the largest change in median RMW is between tropical storm and category 1 intensity and that the change in median RMW from category 3 to 5 is rather small. While we cannot infer how contraction relates to intensity for individual storms from their figure, a plausible interpretation is that, on average, most contraction occurs during the early stages of intensification. Also consistent with this interpretation is Fig. 6 of [Willoughby and Rahn \(2004\)](#), which shows (from flight-level data) RMW as a function of  $V_{max}$  and latitude. It appears from the figure of [Willoughby and Rahn \(2004\)](#) that most of the decrease of RMW with increasing intensity occurs at relatively weak  $V_{max}$ , with a much smaller tendency above about  $30\text{--}40\text{ m s}^{-1}$ . In nature, strong storms are uncommon relative to weaker storms [there were only seven category 5 storms in the dataset of [Kimball and Mulekar \(2004\)](#), for example], and this likely is part of the explanation for why it is widely believed that contraction and intensification always occur together. It may be that for weak storms, contraction is indeed coincident with intensification, and that intensification at a fixed RMW never occurs, simply because major-hurricane status is never achieved.

Using [Vigh's VDM](#) dataset, we can examine the statistical distribution of flight-level RMW as a function of intensity. [Figure 10](#) shows a boxplot of flight-level RMW stratified by best-track Saffir–Simpson category. This is analogous to (and can be compared to) Fig. 15 of [Kimball and Mulekar \(2004\)](#). The largest decrease in median RMW occurs between tropical storms and category 1 hurricanes, similar to [Kimball and Mulekar \(2004\)](#). However, although there is little change in median RMW between category 1 and 2 hurricanes, there is a substantial decrease from category 2 to 3. Further, the 75th percentile RMW decreases noticeably between each successively increasing intensity category. Therefore, the VDM dataset does not yield quite the same result as seen in the EBT data of [Kimball and Mulekar \(2004\)](#). To more clearly indicate how the distribution changes with intensity, in [Fig. 11](#), we show a boxplot of flight-level RMW stratified by the best-track intensity in knots. There is virtually no change in the distribution of RMW from 30 to 50 kt, while the greatest decrease in median RMW is from 50 to 70 kt, consistent with [Fig. 10](#). Again though, there appears to still be a steady decrease in RMW with further increases of intensity, somewhat in contrast to [Kimball and Mulekar \(2004\)](#).

From [Figs. 10 and 11](#), it would seem that, on average, observed tropical cyclones contract throughout their period of intensification. However, the dataset consists of storms at all stages of the TC life cycle, intensifying as well as weakening. A more representative way to assess the distribution of contraction with intensification is to examine the subset of the full dataset where storms are intensifying. [Figure 12](#) is similar to [Fig. 11](#) but only includes data from flight legs where each storm first achieves a given intensity. For example, each of the 80 data points within the 65-kt bin are from a different storm, and each point represents the flight-level RMW when that storm first was observed at an intensity that fell within the 65-kt bin. Therefore, this subset of the data approximately captures the relationship between size and intensity during the initial period of contraction and intensification. [Figure 12](#) shows that the median RMW decreases substantially as intensity increases from 35 to 65 kt but that further increases in intensity yield (on average) relatively little further contraction. At 95 kt and beyond, the distribution of RMW is nearly constant with intensity. This indicates that for storms that become major hurricanes, most contraction is completed prior to much of the intensification. To the extent that we can make a comparison, this behavior is consistent with our numerical simulations.

#### 4. What drives contraction?

In the convective ring model, it is the secondary circulation induced by condensational heating that causes

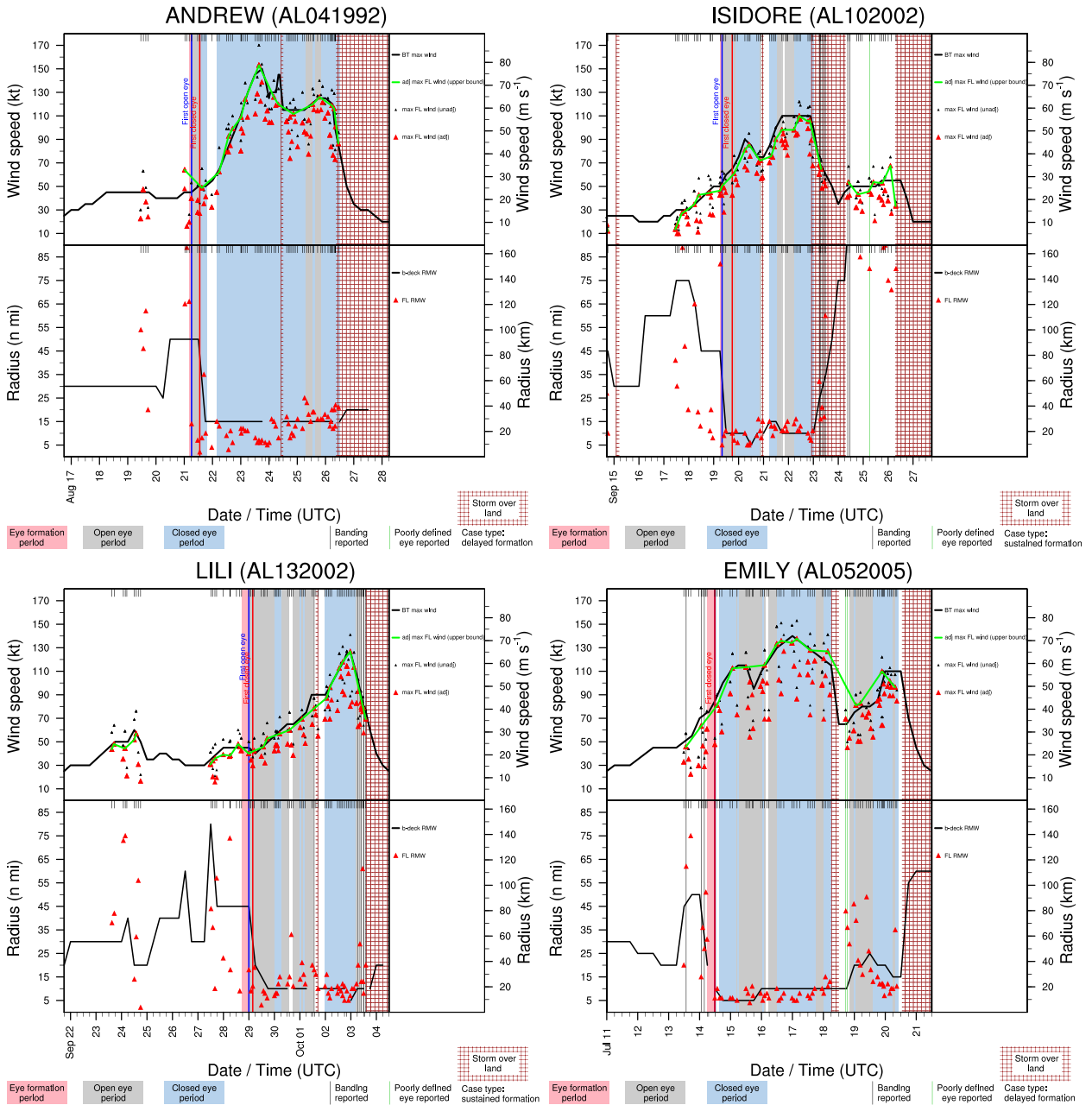


FIG. 8. Time series of (top)  $V_{max}$  and (bottom) RMW for selected observed storms for which most intensification occurs subsequently to most contraction. Shown are Andrew (1992), Isidore (2002), Lili (2002), and Emily (2005). The data for these time series come from the VDMs transmitted in real time from Air Force and NOAA Hurricane Hunter aircraft. (top) The maximum flight-level wind for each flight is indicated by the black triangles, while the red triangles indicate these winds adjusted to the surface. The green line is fit to the upper bound of the surface-adjusted flight-level maxima. The best-track  $V_{max}$  is plotted in black. (bottom) The flight-level RMW from the VDMs is indicated by red triangles, and the “b-deck” RMW recorded by NHC is plotted in black. Details on the construction of these plots can be found in [Vigh \(2010\)](#).

contraction, as the associated tangential wind tendency is maximized inward of the RMW. Here, we investigate the role of both symmetric heating and friction in driving contraction, using the linear vortex model 3-Dimensional Vortex Perturbation Analysis and Simulation (3DVPAS; [Nolan and Montgomery 2002](#); [Nolan and Grasso 2003](#)).

3DVPAS is a dry, nonhydrostatic model that can be used to solve for the time-evolving response of a vortex to imposed forcings. Starting from a basic-state flow that is fixed in time (as the model is linear), the perturbation flow induced by either heat or momentum sources can be determined. This is similar (in result) to solving

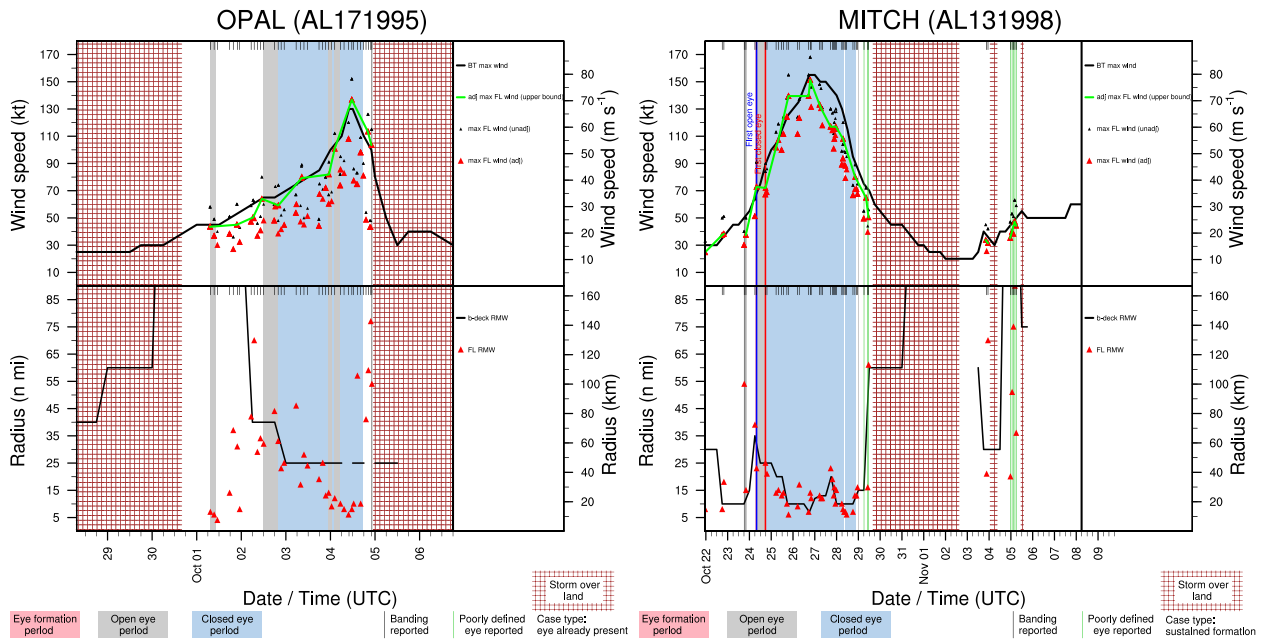


FIG. 9. As in Fig. 8, but for selected observed storms for which most intensification occurs concurrently with most contraction. Shown are Opal (1995) and Mitch (1998).

a diagnostic Sawyer–Eliassen equation, which has been used in a number of studies (e.g., Bui et al. 2009). In particular, 3DVPAS yields a very similar result to the analytical solutions of the Sawyer–Eliassen equation given in Schubert et al. (2007, hereafter S07) and Rozoff et al. (2008) (demonstrated in the appendix). A more complete description of 3DVPAS can be found in Hodys and Nolan (2007) and Nolan et al. (2007).

Here, we use 3DVPAS to calculate the tangential wind tendency and secondary circulations induced by symmetric heating and by friction in our idealized WRF simulation. The WRF output provides both the basic-state vortex and the forcing. Figure 13a shows the 12-h time-averaged azimuthal-mean tangential wind for 0000–1200 UTC day 2 in the control simulation. This time is chosen because it is during the period of rapid contraction of the RMW. Although the prognostic equations of 3DVPAS impose no constraint of balance on the solution, the basic-state vortex does need to be balanced, and 3DVPAS will generate the temperature and pressure fields that are in thermal wind balance with the prescribed wind field. The tangential wind field in WRF (and in real storms) is characterized by an unbalanced boundary layer, where winds decrease downward toward the surface. So if we use the WRF tangential wind field as the basic-state vortex, 3DVPAS will balance this boundary layer flow with a strong negative temperature perturbation that does not exist in the actual WRF fields. Therefore, we instead use the gradient wind field as our basic state (Fig. 13b), modestly horizontally and vertically smoothed (20 and 40

times, respectively, with a 1–2–1 smoother), and with the gradient winds made to be constant with height below 500 m. It can be seen that above the boundary layer, the gradient wind is very similar to the actual tangential wind. The 12-h time-averaged WRF diabatic heating and PBL tangential wind tendency are shown in Figs. 13c and 13d, respectively. The diabatic heating comes from direct model output from the WSM6 microphysics scheme, and the PBL term is the parameterized frictional tendency on tangential winds from the YSU scheme. We use these time-averaged tendencies as constant forcings for 3DVPAS. The RMW of the time-averaged gradient wind (from Fig. 13b) is also plotted in Figs. 13c and 13d, and it is evident that both the heating and the frictional tendency are maximized inward of the RMW.

After integrating 3DVPAS forward in time for 6 h, a quasi-steady-state secondary circulation is achieved.<sup>7</sup> Figure 14a shows the 3DVPAS-calculated azimuthal-mean

<sup>7</sup> We use 6 h because at longer times, the secondary circulation near the lower boundary slowly changes, and this tendency is sensitive to the magnitude of numerical diffusion in 3DVPAS. After careful evaluation, we chose 6 h as a representative time at which the secondary circulation has become quasi steady and prior to the long-term evolution. For these calculations, the 3DVPAS domain extends to 540 km in the radial direction and 18 km in the vertical, with  $135 \times 40$  radial and vertical grid points, respectively. The radial grid spacing is constant at 4 km, while the vertical grid is stretched, with 240-m grid spacing near the surface and a maximum grid spacing of 600 m.

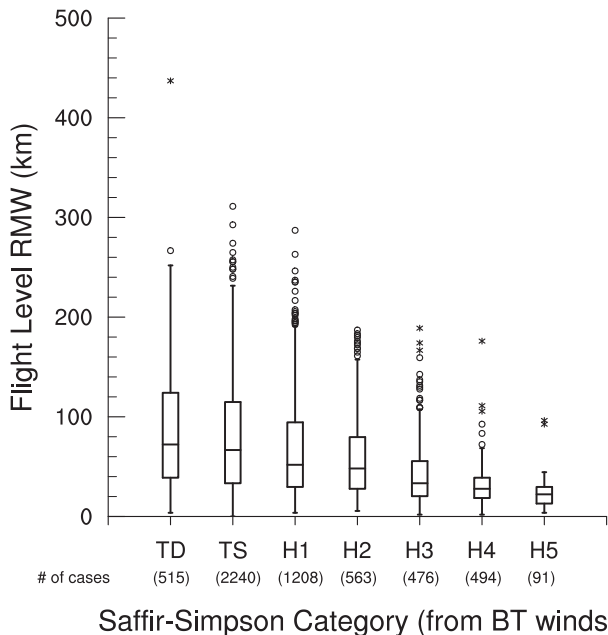


FIG. 10. Boxplot of the RMW at flight level (from the VDM dataset), stratified by the best-track Saffir-Simpson category. The median is given by the horizontal line within the box, and the top and bottom edges of the box indicate the 25th and 75th percentiles, respectively. The “whiskers” extend to the highest and lowest values that are found within a distance of 1.5 times the interquartile range from the top and bottom edges of the box, respectively. Outliers that are between a distance of 1.5 and 3 times the interquartile range from the edges of the box are indicated with circles. “Far outliers” that are at a distance greater than 3 times the interquartile range from the edges of the box are indicated by asterisks. The sample size for each intensity category is indicated parenthetically beneath the plot.

radial velocity induced by the combination of diabatic heating and friction, along with  $10 \text{ cm s}^{-1}$  contours of the azimuthal-mean vertical velocity, representing the eyewall. This can be compared to the actual 12-h-mean fields from WRF, shown in Fig. 14b. Figures 15a and 15b show analogous plots for the azimuthal-mean vertical velocity. The 3DVPAS solution compares qualitatively (and even quantitatively) quite well to the actual WRF secondary circulation, validating 3DVPAS, and confirming that the secondary circulation is indeed largely the balanced response to symmetric forcing. The position and shape of the eyewall in 3DVPAS are basically correct, as are the depth of the layer of strong inflow, the layer of deeper weak inflow, and the upper-level outflow layer. It can be seen that the secondary maximum of outflow in the low-level eyewall evident in the WRF simulation is absent in 3DVPAS. This latter feature is seen in numerous full-physics simulations as well as in observations (Schwendike and Kepert 2008; Zhang et al. 2011) and is the result of unbalanced dynamics [first

shown in Kepert and Wang (2001)]. Since we are not directly including friction itself in 3DVPAS (only the resulting tendency on tangential wind as a forcing), we would not expect to reproduce this feature. Additionally, the upper-level subsidence in the eye is too strong in 3DVPAS, as is the associated upper-level inflow just inward of the eyewall. Nevertheless, it is clear that 3DVPAS is able to generally reproduce the secondary circulation, which is responsible for spinning up the tangential wind field, through angular momentum advection.

As 3DVPAS is a linear model, the effects of heating and friction are additive, and so we can examine them individually as well. Figures 14c,d and 15c,d show the secondary circulation induced by the effects of heating and friction alone, respectively. The eyewall updraft, upper-level outflow layer, and deep inflow layer are almost entirely due to diabatic heating.<sup>8</sup> The effects of friction are only significant in the lowest 4 km, with a 3-km-deep layer of weak outflow overlying a 1-km-deep layer of stronger inflow. Although it is commonly assumed that friction is overwhelmingly responsible for the boundary layer inflow, and there are a number of recent studies that take for granted that this is the case (e.g., Smith et al. 2009; Abarca and Montgomery 2013), it can be seen here that diabatic heating is actually responsible for a substantial portion of this inflow. In fact, here friction is only responsible for 50%–60% of the inflow near the RMW at the lowest 3DVPAS level (120 m), with 40%–50% contributed by heating. Further, the layer of stronger inflow induced by heating is substantially deeper than that induced by friction, and above 1 km, the “frictional inflow layer” is almost entirely due to diabatic heating.

The radial and vertical flow yields a tangential wind tendency, through the advection of absolute angular momentum. Figure 16a shows this calculated tendency in 3DVPAS from the secondary circulation induced by the combined heating and friction. Note that friction exhibits a direct tendency on the tangential wind as well (and this is the forcing, shown in Fig. 13d). We therefore have included this frictional spindown as part of the net tendency for 3DVPAS shown in Fig. 16a. The actual change in tangential winds in WRF over this time period is shown in Fig. 16b. There is a fair qualitative agreement between 3DVPAS and the actual tendency field in the

<sup>8</sup> This result appears to disagree with Schubert and McNoldy (2010), who found that for strong-enough vortices, frictionally induced updrafts can extend to the tropopause. The reason for this discrepancy is unclear, though we speculate that it may have to do with the fact that Schubert and McNoldy (2010) specify the radial profile of  $w$  at 1-km height, whereas in our case,  $w$  is a response to the momentum forcing (taken from the PBL scheme).

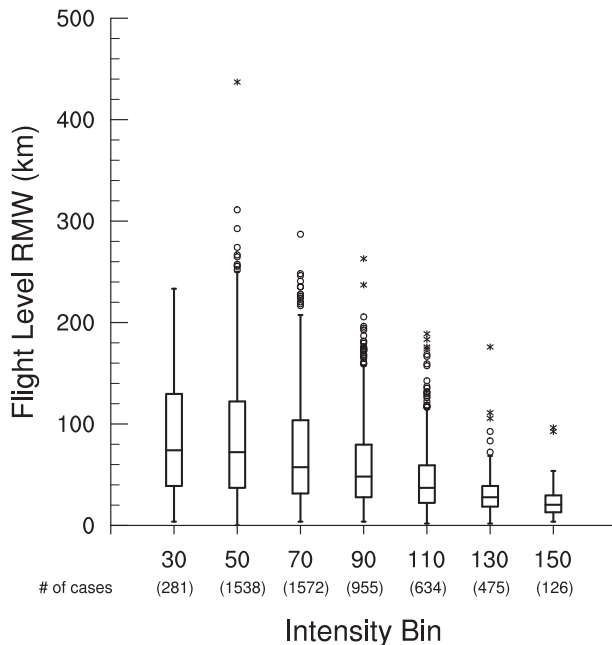


FIG. 11. As in Fig. 10, except stratified by best-track intensity (kt), using an equal bin size. The intensity labeled below each box is the upper limit of intensity (e.g., “30” uses all cases where the intensity is less than 30 kt, “50” uses all cases where the intensity is between 30 and 50 kt, etc.). Note that in constructing this plot, best-track intensity has been interpolated to the time of each VDM observation.

eyewall, though there are some substantial quantitative differences. The maximum tangential wind tendency is found inside of the initial RMW, consistent with the WRF simulation, though the location of the maximum in 3DVPAS is about 5 km radially outward of that in WRF. Overall, the computed tendency in 3DVPAS in the eyewall is too large, especially at low levels. In 3DVPAS, there is also a secondary upper-level maximum in wind tendency and a spindown of the winds in the eye, neither of which are found in WRF. These discrepancies are likely due to a number of factors, including the effect of horizontal diffusion in WRF and the neglect of nonlinear dynamics in 3DVPAS. However, the basic structure of an annulus of positive wind tendency that is maximized inward of the RMW and at low levels is reproduced by 3DVPAS.

As with the secondary circulation, we can partition the tangential wind tendency into components associated with heating (Fig. 16c) and those associated with friction (Fig. 16d). Consistent with Figs. 14 and 15, Fig. 16 shows that the spinup of the tangential wind field is at most heights due almost entirely to diabatic heating. Diabatic heating dominates the tendency even in the boundary layer, and spinup is maximized in this region in response to heating and not friction. In fact, the net frictional tendency on tangential winds is negative. This is because

even though friction induces inflow that yields a large positive tendency (Fig. 17), the direct spindown of the winds by friction more than offsets the tendency from frictional inflow. This stands in contrast to several recent studies that have concluded that the boundary layer winds in tropical cyclones are spun up by friction (Smith et al. 2009; Abarca and Montgomery 2013, 2014). However, our results indicate that the net effect of friction on the tangential winds is indeed negative. The net effect of friction contributes to the contraction of the RMW within the boundary layer (though the effect of heating is dominant), because the negative tendency on winds is maximized at or just outside of the RMW, and therefore  $(\partial/\partial r)(\partial V/\partial t)$  is negative.

## 5. Summary and discussion

### a. Summary

In this study, we have reexamined the relationship between the intensification of the maximum winds and the contraction of the radius of maximum winds (RMW) within tropical cyclones. From idealized simulations, we found that, in general, most contraction occurs prior to most intensification, and a quasi-steady size is often reached well before a quasi-steady intensity is achieved. In these simulations, the RMW first propagates inward across  $M$  surfaces, moving from higher to lower values of  $M$  during the initial period of rapid contraction. Once contraction of the RMW ceases,  $M$  surfaces propagate inward across the RMW, as intensification continues “in place.” By varying the initial RMW, we showed that this phenomenon occurs in storms of differing size. Contraction is slower in initially larger storms, and as the time period of contraction is also longer, the lag between the times at which quasi-steady size and quasi-steady intensity are reached becomes smaller with increasing initial RMW. Nevertheless, in the larger storms, most of the contraction of the RMW still occurs prior to most of the intensification.

From a kinematic perspective, the rate of contraction of the RMW is a function of the radial gradient of the wind tendency  $(\partial/\partial r)(\partial V/\partial t)$  and the degree to which the profile of tangential winds is peaked, as represented by its curvature  $\partial^2 V/\partial r^2$ , both evaluated at the RMW itself. In our simulations, contraction begins and subsequently accelerates as a result of an increase in the radial gradient of the wind tendency. This phase of accelerating contraction occurs both prior to and during the early portion of the rapid intensification (RI) period of the tropical cyclone. At a certain time, the inward propagation of the RMW rapidly slows down and is later halted. It is the rapid increase in curvature that is responsible for the slowing of contraction and not changes

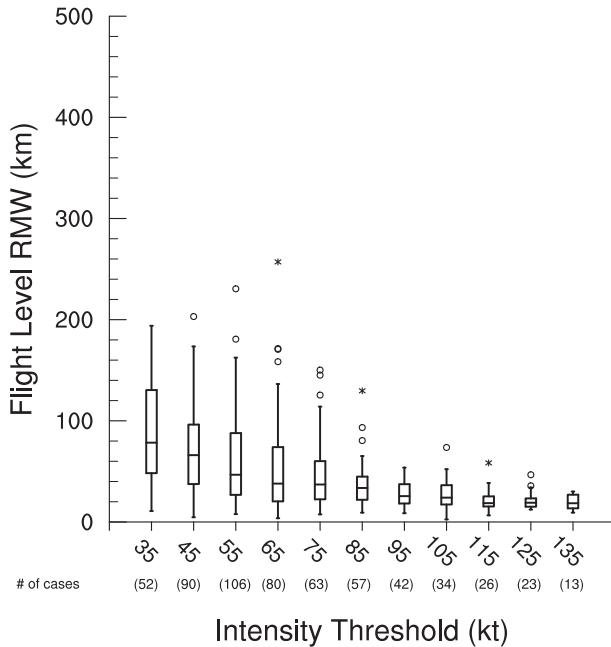


FIG. 12. As in Fig. 11, except only using data from flight legs where each storm first achieves a given intensity (see text). The intensity labeled below each box is the upper limit of intensity (e.g., “35” uses all cases where the intensity is less than 35 kt, “45” uses all cases where the intensity is between 35 and 45 kt, etc.). Note that in constructing this plot, best-track intensity has been interpolated to the time of each VDM observation.

in the radial gradient of the wind tendency (which would otherwise favor continued contraction). In our simulations, the sharpness of the RMW continues to increase following the halting of contraction. This effectively prevents any further significant contraction or expansion of the RMW, despite the existence of periods where the radial gradient of the wind tendency is as large as during the period of rapid contraction.

Many observed storms exhibit a similar relationship between contraction and intensification as is seen in our simulations. This stands in contrast to the widely believed paradigm whereby the RMW contracts as it maintains a constant value of  $M$ , with intensification occurring simultaneously. We presented examples of storms that appear to have an intensification–contraction relationship that is similar to what is shown in our simulations, as well as storms that appear to contract near simultaneously with intensification. We also showed that the observed statistical distribution of size as a function of intensity implies that, on average, contraction is largely complete prior to the end of intensification. As a result of limited spatial and temporal sampling, it is difficult to conclude which mode of contraction is more prevalent in the observations. Nevertheless, it seems that a substantial

number of observed storms behave consistently with our simulations.

We investigated the dynamical mechanisms of contraction and intensification by taking the diabatic heating and frictional tendencies from a WRF simulation as a fixed-in-time forcing for a linearized vortex model: 3DVPAS. Integrating 3DVPAS forward in time with the WRF forcing yields the quasi-steady-state secondary circulation that is induced by the forcing. We showed that 3DVPAS is able to qualitatively reproduce the secondary circulation from the WRF simulation rather well. Examining the separate responses to heating and friction, we found that heating is responsible for nearly all of the inflow above 1-km height, which includes the upper portion of the layer of stronger “boundary layer” inflow. Below 1-km height, heating and friction both contribute substantially to inflow.

The tangential wind tendency associated with the secondary circulation in 3DVPAS compares well in a qualitative sense with the actual change in WRF tangential winds, albeit with substantial quantitative differences. From the 3DVPAS tendencies, we found that the spinup of the tangential wind near the RMW is at most heights nearly entirely associated with diabatic heating. This is true even in the boundary layer, as the net frictional tendency in this region is negative. While friction does induce inflow that yields positive tangential wind tendencies, this is outweighed by the direct spin-down effect. Interestingly, both heating and friction contribute to the contraction of the RMW: eyewall heating contracts the RMW because the positive tangential wind tendency is maximized inside of the RMW, while boundary layer friction contracts the RMW because the negative tangential wind tendency is maximized outside of the RMW.

*b. Discussion*

As far as we are aware, SN11 first identified the phenomenon in simulations of tropical cyclones whereby contraction of the RMW achieves completion well before rapid intensification has ended. However, it is apparent from a survey of the literature that a number of simulations examined in previous studies (as cited in section 2 and in SN11) exhibit evidence of this behavior, although the authors did not appear to realize it. Therefore, we are quite confident that this relationship between contraction and intensification is indeed robust and is not due to anything peculiar to our modeling framework. As a number of observed storms also exhibit contraction of the RMW that halts in the middle of RI, it is clear that the simulated behavior occurs in real tropical cyclones as well. It remains unclear how typical it is for the RMW to reach a steady state prior to peak

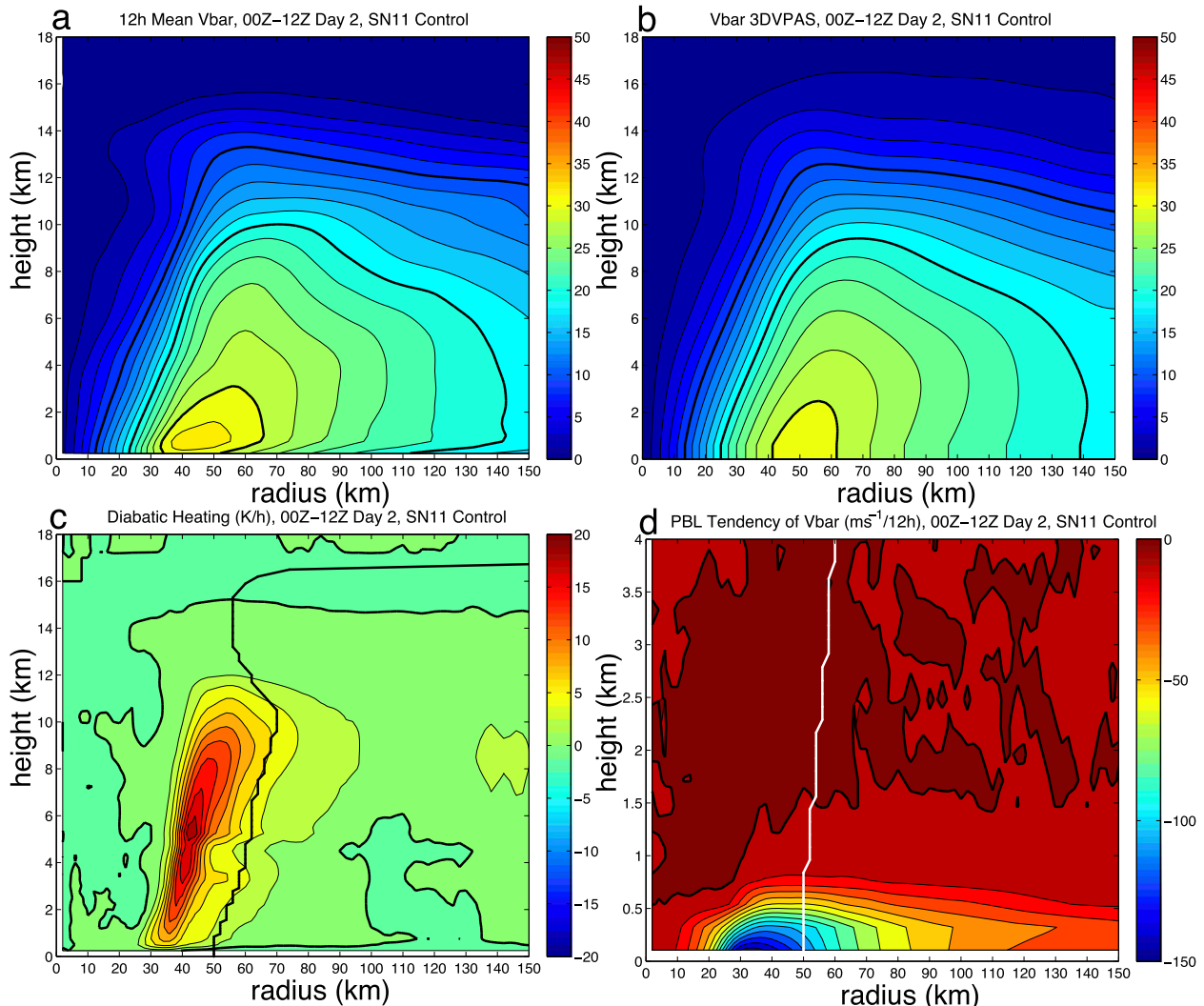


FIG. 13. (a) Azimuthal-mean tangential wind from the control simulation, contoured every  $2 \text{ m s}^{-1}$  with every  $10 \text{ m s}^{-1}$  thickened. (b) As in (a), but for the gradient winds. In (b), modest radial and vertical smoothing has been applied, and the winds are set constant below  $z = 500 \text{ m}$ . The wind field in (b) is the basic-state vortex used in all calculations with 3DVPAS. (c) Azimuthal-mean diabatic heating from the WSM6 microphysics scheme, contoured every  $2 \text{ K h}^{-1}$ , with the zero contour thickened. (d) The azimuthal-mean tendency on tangential winds from the YSU PBL scheme, contoured every  $10 \text{ m s}^{-1} (12 \text{ h})^{-1}$ , with the zero contour thickened. In all panels, the respective fields represent 12-h time averages for 0000–1200 UTC day 2, using 6-min data. In (c) and (d), the RMW defined from the wind field in (b) is plotted in black and white, respectively. Note that the y axis in (d) is different from the other panels.

intensity, as opposed to following the existing paradigm, where peak intensity is coincident with the end of contraction. Currently, it appears that both types of behavior exist to some degree in nature. In the future, we plan to more comprehensively address this question, using the vortex data messages as well as flight-level wind profiles.

In Stern and Nolan (2009) and Stern et al. (2014), it was shown that in observed storms, the RMW can be approximated as an  $M$  surface, although  $M$  decreases systematically with height along the RMW (on average by 8% from 2- to 8-km heights). It is therefore

reasonable to think of the RMW as an  $M$  surface at any given time. The results of this study show that it is not correct to assume that the same  $M$  surface remains associated with the RMW at all times. It is possible that  $M$  could be perfectly conserved, and the RMW could be at all times coincident with an  $M$  surface, but this does not mean that the RMW must propagate as an  $M$  surface. Interestingly, there is some evidence that in highly idealized models, the RMW does maintain nearly constant  $M$  with time, and intensification is therefore synonymous with contraction. Mrowiec et al. (2011) simulated dry axisymmetric hurricanes by imposing large air–surface

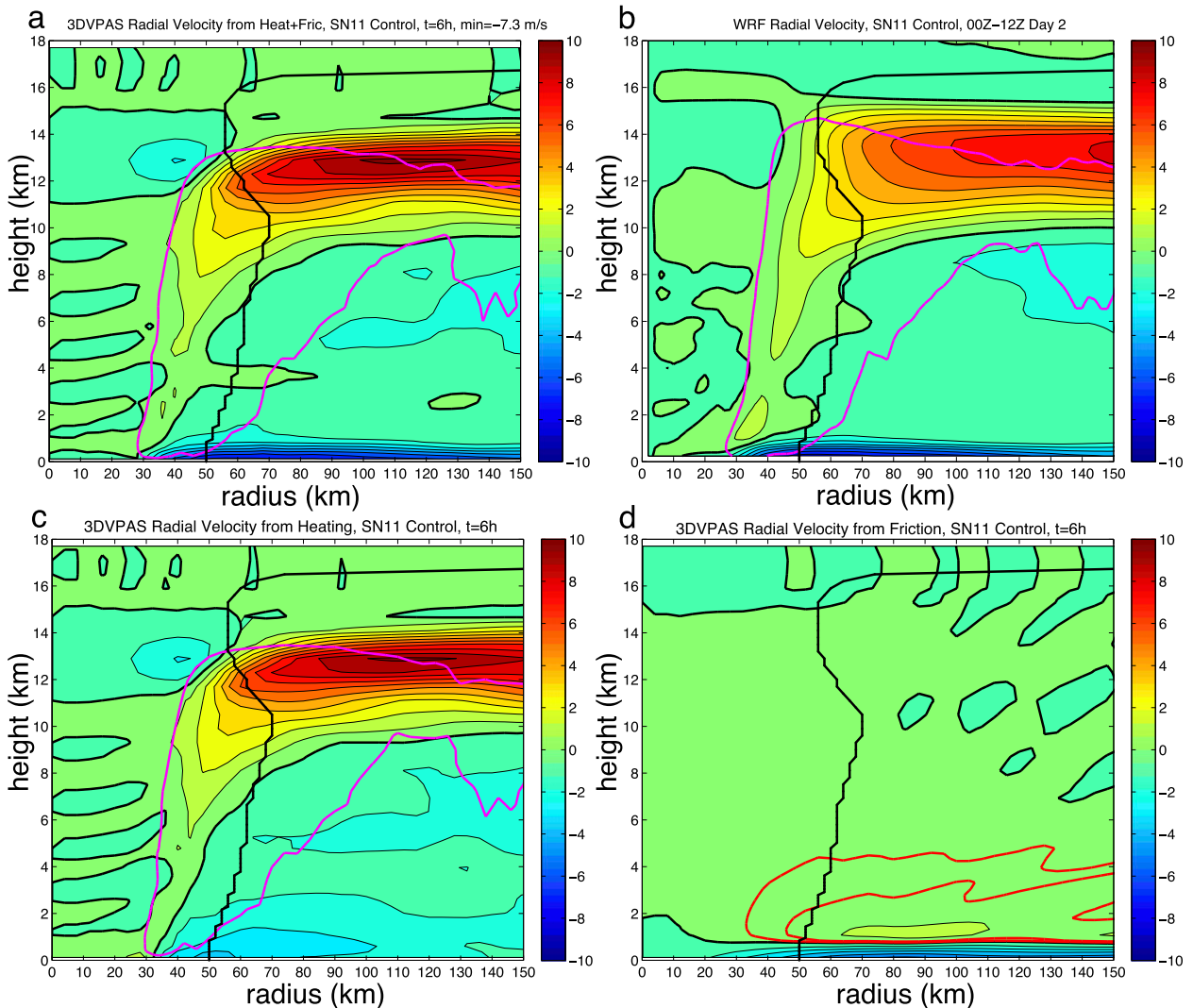


FIG. 14. (a) Radial velocity from 3DVPAS, forced by heating and friction from the control WRF simulation for 0000–1200 UTC day 2. (b) The actual WRF radial velocity. (c) Radial velocity from 3DVPAS, forced by heating from WRF. (d) Radial velocity from 3DVPAS, forced by friction from WRF. In (a) and (c), the  $10 \text{ cm s}^{-1}$  azimuthal-mean updraft from the respective 3DVPAS calculation is contoured in magenta [in (d), the peak vertical velocity is less than  $10 \text{ cm s}^{-1}$ ]. In (b), the actual WRF vertical velocity is contoured in magenta. In (d), the  $0.25$  and  $0.50 \text{ m s}^{-1}$  radial outflow is contoured in red. In all panels, the contour interval of radial velocity is  $1 \text{ m s}^{-1}$ , the zero contour is thickened, and the RMW based on the flow in Fig. 13b is shown in black.

temperature differences. They found a one-to-one relationship between RMW and  $V_{\text{max}}$  among their dry simulations, and the authors stated that the RMW approximately maintains constant  $M$ . This relationship is absent in similar moist simulations that they performed. The nearly constant  $M$  with time seen in the dry simulations of Mrowiec et al. (2011) is also found in the simple axisymmetric model of Emanuel (1995), as shown in Stern and Nolan (2009). This implies that perhaps the presence of moist convection fundamentally alters the manner in which contraction occurs.

Recently, Kieu (2012) showed that for a WRF ensemble of simulations of Hurricane Katrina (2005),<sup>9</sup> each ensemble member halted contraction in the middle of RI, well before peak intensity was achieved. They also noted, “The slowing down of the RMW contraction at the middle of the intensification appears to be a common characteristic of the hurricane development.” The focus of their study was to develop

<sup>9</sup>A similar set of simulations was originally conducted and examined by Weng and Zhang (2012).

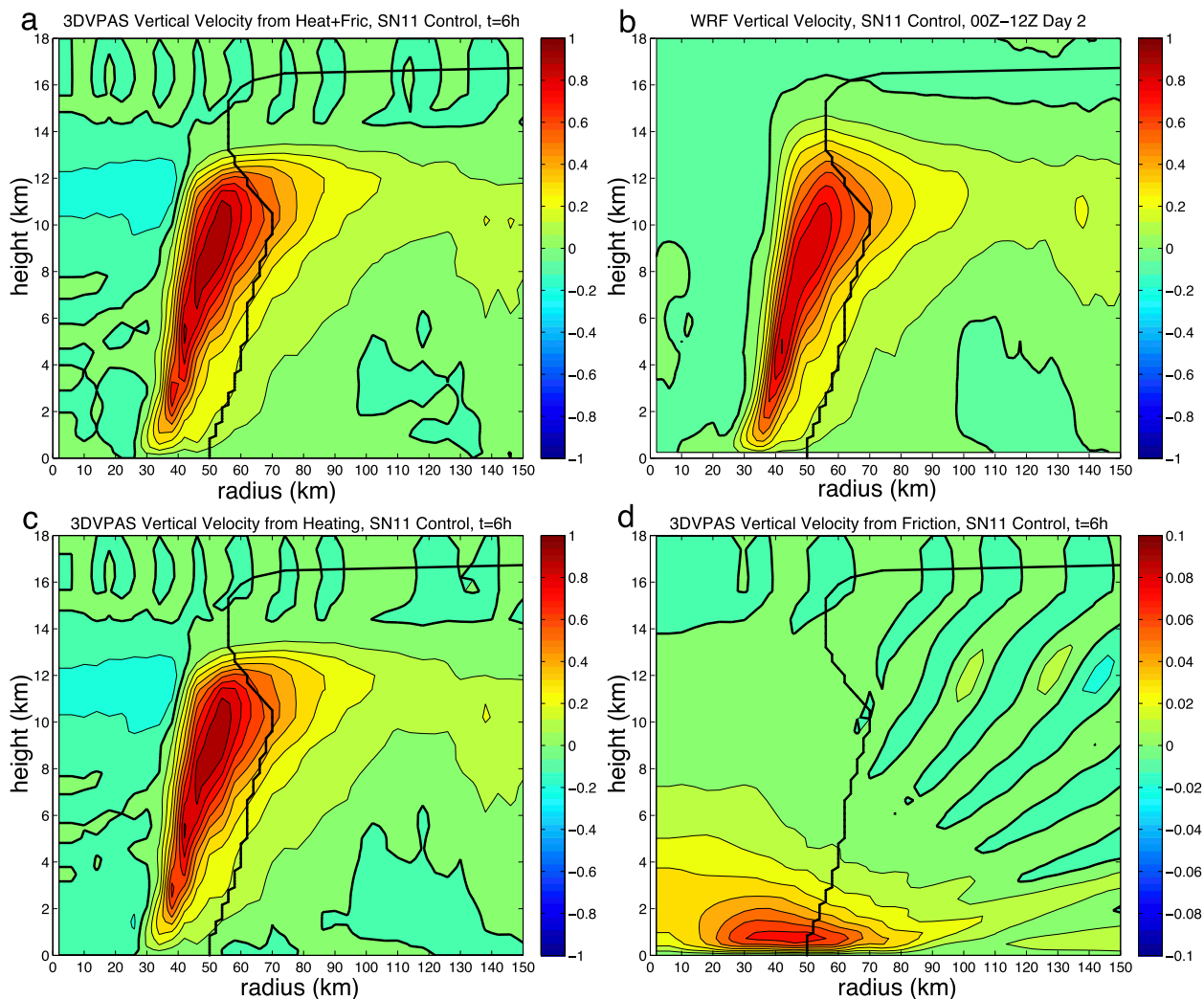


FIG. 15. (a) Vertical velocity from 3DVPAS, forced by heating and friction from the control WRF simulation for 0000–1200 UTC day 2. (b) The actual WRF vertical velocity. (c) Vertical velocity from 3DVPAS, forced by heating from WRF. (d) Vertical velocity from 3DVPAS, forced by friction from WRF. In (a)–(c), the contour interval of vertical velocity is  $0.1 \text{ m s}^{-1}$ , while in (d) the contour interval is  $0.01 \text{ m s}^{-1}$ . In all panels, the zero contour is thickened, and the RMW based on the flow in Fig. 13b is shown in black.

a “kinematic model of the RMW contraction.” Unfortunately, this model of contraction does not appear to be correct.<sup>10</sup> Kieu (2012) starts from the viewpoint that the RMW can be advected (which, as discussed in section 2, is incorrect) and then attempts to formulate an equation for contraction that is based on a presumed balance between advection and friction. As Kieu (2012) states,

<sup>10</sup> There is a mathematical error in the derivation of Kieu (2012). Kieu (2012) substitutes his (2) into his (4) to get (5) but leaves out the term  $\Omega dR/dt$ . As a result, the  $Rd\Omega/dt$  term cannot actually be eliminated as he does to get his (6), and so his final solution for  $dR/dt$  is incorrect.

“That the RMW locates consistently in the inflow regime implies that the frictional forcing must play some role in preventing the inward advection of the RMW by the radial inflow.” In addition to neglecting other possibly important forces, the implication of this statement is that inflow would forever contract the RMW if not for friction, and so there must be some sort of balance at this radius in order for the RMW to be steady.

While the sum of all forcings (including radial advection and friction) that contribute to the tangential wind tendency does indeed determine the rate of change of the RMW, from a kinematic perspective, contraction is a function only of the tangential wind near the RMW and its radial and time derivatives. The

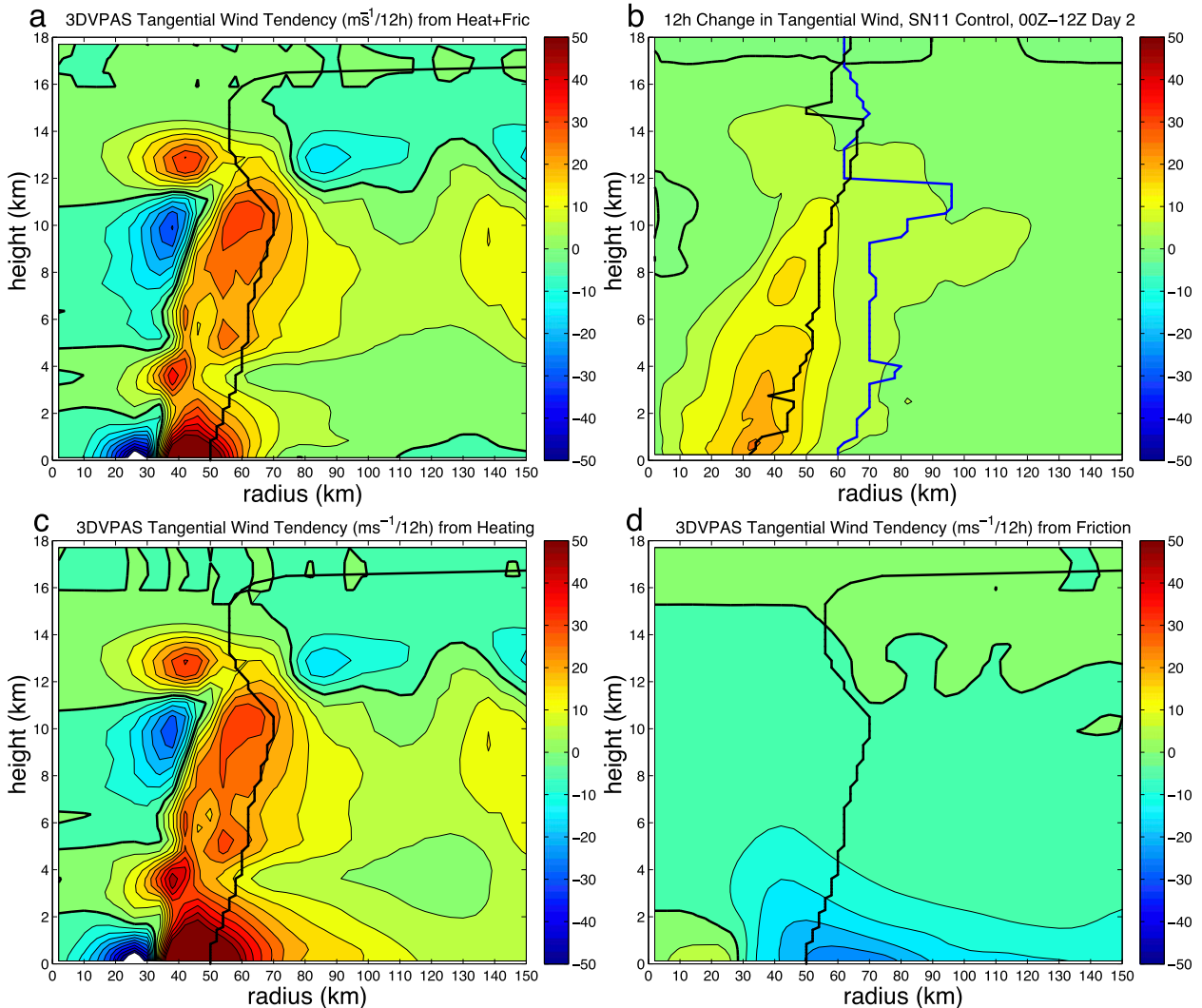


FIG. 16. (a) Tangential wind tendency from 3DVPAS, forced by heating and friction from the control WRF simulation for 0000–1200 UTC day 2. (b) The actual 12-h change in tangential wind in the WRF simulation for 0000–1200 UTC day 2. (c) As in (a), but for heating alone. (d) As in (a), but for friction alone. In (d), the tendency shown is the sum of the frictional forcing itself and the tendency that is a response to friction. In all panels, the contour interval is  $5 \text{ m s}^{-1} (12\text{h})^{-1}$ , and the zero contour is thickened. For (a),(c), and (d), the RMW based on the flow in Fig. 13b is shown in black. In (b), the RMW (from the actual wind field) at the start and end of the 12-h period is shown in blue and black, respectively.

RMW is not itself a material surface that can be advected, and so it is not meaningful to refer to a balance between friction and advection in this context. The direct effect of friction exerts a negative tendency on tangential wind, and since this negative tendency is maximized inward of the RMW in our simulations, this would, on its own, act to oppose contraction. The key point is that contraction does not depend on whether the wind tendency is positive or negative; all that matters is whether the radial gradient of the tendency (at the RMW) is positive or negative. For example, during the period of rapid contraction in our

simulation, the net effect of friction (including frictional inflow) is actually to contract the RMW, since the radial gradient of the tangential wind tendency at the RMW (in the boundary layer) is negative.<sup>11</sup> Radial advection and surface friction do affect the radial

<sup>11</sup> There is another reason that we do not necessarily have to invoke friction in order to explain why radial inflow does not advect  $M$  surfaces inward until the point of singularity. In tropical cyclones, radial inflow does not penetrate inward to the center of rotation but instead is halted at a finite radius.

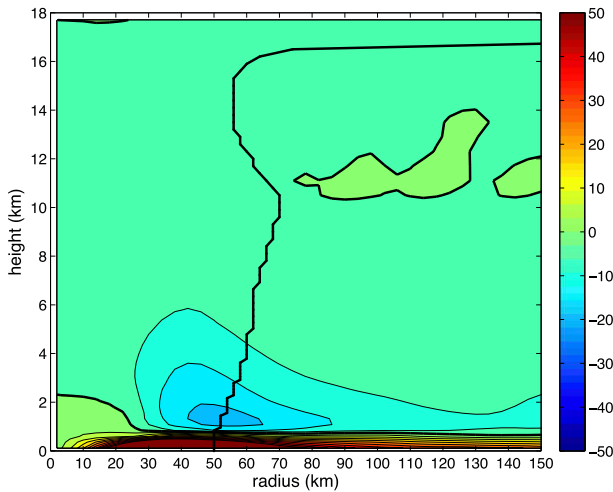


FIG. 17. As in Fig. 16d, but for the tangential wind tendency due to frictional inflow alone, not including the contribution from the direct spin-down effect of friction.

profile of tangential wind, but the radial structure of these terms, along with the radial structure of the tangential winds, are needed in any type of dynamical analysis. As Kieu’s analytical model does not predict these, it cannot be used to understand the dynamics or kinematics of contraction. While the model of Kieu (2012) does not succeed in explaining contraction, their study does lend further support to the idea that contraction often ceases prior to the end of RI.

In a series of recent studies, Bryan and Rotunno (2009), Bryan (2012), and Rotunno and Bryan (2012) examined tropical cyclones in axisymmetric numerical simulations. While their primary focus was on the maximum simulated intensity, they also examined various aspects of storm structure, including the RMW. Bryan and Rotunno (2009) and Bryan (2012) found that the quasi-steady-state RMW of the simulated storms increased systematically with increasing parameterized horizontal diffusion, as given by the horizontal mixing length  $l_h$ . Based on a momentum budget analysis, Rotunno and Bryan (2012) found that near the radius and height of maximum winds, quasi-steady  $M$  was largely determined by a balance between radial advection and horizontal diffusion. They argued that with larger diffusivity,  $M$  surfaces become spread out in such a way so that the RMW is located at larger radius. Finally, they developed a simplified analytical model for the steady-state profile of  $M$ , given a balance between horizontal advection and horizontal diffusion and a specified radial profile of  $u$ , and found that the RMW increased with increasing diffusivity,

which is consistent with the numerical simulations of Bryan (2012).<sup>12</sup>

The aforementioned studies provide evidence for the dynamical mechanisms that govern the quasi-steady size of the RMW and so are not necessarily inconsistent with our results in section 2, which present a kinematic perspective on contraction. We showed that if the radial gradient of the tangential wind tendency is negative at the RMW, then the RMW must be contracting, regardless of the dynamical reasons for this gradient. Diffusion and advection may indeed be determining the sign and magnitude of this gradient. However, contraction by definition is occurring when the tropical cyclone is not in a steady state, and it is possible that other mechanisms (such as surface friction, as we showed in section 4) also are involved in driving contraction. Finally, we speculate that although horizontal diffusion may (in part) govern the minimum possible size of the RMW, it is possible that increased diffusion actually increases the rate of contraction. This is because diffusion will generally lead to a more rounded radial profile of tangential wind near the RMW, which (as shown in section 2) increases the rate of contraction. This hypothesis can be tested in future studies.

Bui et al. (2009) used the Sawyer–Eliassen equation to examine the effect of heating and friction on driving a secondary circulation, using output from the MM5 simulation of Van Sang et al. (2008). While in our study, we found that the linear response of a balanced vortex to heating and friction is able to quantitatively reproduce the simulated secondary circulation, Bui et al. (2009) found that the low-level inflow in their calculation was weaker by a factor of 3 than the actual MM5 inflow. They concluded that this “missing” inflow must be due to unbalanced dynamics and that, therefore, the majority of the spinup of tropical cyclones is fundamentally unbalanced. In our view, this conclusion is unwarranted, and there can be other reasons why the inflow is underestimated. For example, Bui et al. (2009) used a temperature field that is in balance with the actual wind field, which yields a fictitious cold core in the boundary layer. In an appendix, they presented the result of a calculation using the actual temperature field instead, and they found that the low-level inflow was increased by a factor of 2. In our calculations, we use the temperature field that is in balance with the gradient wind field. We conducted a sensitivity test (not shown)

<sup>12</sup> Note that the role of horizontal diffusion in governing size shown by the aforementioned studies is fundamentally different from the proposal by Kieu (2012) that surface friction controls the size of the RMW.

using the temperature field that is in balance with the actual tangential wind field, and this yields substantially reduced inflow, consistent with the sensitivity seen in Bui et al. (2009). Apparently, it is indeed possible to reproduce the low-level inflow in simulated TCs as the combined response of a balanced vortex to heating and friction, and this casts doubt on recent theories that appeal to unbalanced dynamics to explain intensification.

Several recent papers (e.g., Smith et al. 2009; Abarca and Montgomery 2013, 2014), have proposed that the spinup of the inner core of tropical cyclones is largely a result of frictionally driven inflow in the boundary layer as opposed to spinup occurring through a deep layer of heating-induced inflow. These studies argue that the inflow that is induced by friction is large enough such that the associated radial momentum advection outweighs the direct negative (spin down) effect of friction. As far as we are aware, no study has yet to actually demonstrate this; that is, no such study has compared the positive tendency on tangential winds due to frictional inflow with the negative tendency on tangential winds due to friction itself.<sup>13</sup> We found that in our WRF simulation, the direct frictional spindown of tangential winds (as given by the PBL parameterization) is of greater magnitude than the spinup of tangential winds from the frictionally induced inflow. At least in this case, surface friction does not spin up the inner-core wind field; rather, it is a net sink of angular momentum and spins down the inner-core wind field. If friction has a net negative effect on spinup, then it must be diabatic heating that is actually responsible for spinup. As we have shown, heating-induced inflow can be quite large within the boundary layer, and it is actually maximized there. Friction is still quite important for spinup, as it largely determines where boundary layer convergence and vertical motion are maximized, and therefore where eyewall clouds and heating occur (Kepert and Nolan 2014). However, our results show that the spinup of the tangential wind field is largely driven by eyewall heating and not by frictional processes.

Although we now have a better understanding of the kinematics of contraction of the RMW, the dynamical reasons for why the RMW stops contracting during the middle of RI remain unknown. In our simulations, the rapid sharpening of the tangential wind field halts

contraction, but it is unclear as to why this happens when it does. One possible clue is that the contraction of the eyewall updraft appears to slow down and stop about 12 h prior to the analogous behavior of the RMW. As the position of the eyewall updraft is strongly controlled by frictional dynamics (Kepert 2013; Kepert and Nolan 2014), perhaps the boundary layer plays an important role. In his observational study, Vigh et al. (2012) found that “once the eye forms, both the median Rmax and median eye diameters settle into a narrow range, with just a slow decrease even as the eye reaches greater definition.” It is possible that the formation of the eye itself is closely related to the dynamics of eyewall contraction. This study is a first step toward understanding these relationships, and in future work, we hope to provide answers to some of the remaining mysteries of the hurricane eye.

*Acknowledgments.* The authors thank three anonymous reviewers for their beneficial comments and suggestions. The first author also thanks Michael Stern for helpful discussions. During various stages of this study, support to Daniel Stern was provided by a University of Miami graduate fellowship; an NSF-AGS Postdoctoral Research Fellowship (AGS-1231193); NSF Grants ATM-0432551, ATM-063064, and ATM-0840651; ONR Grant N000140910526; and NOAA (HFIP).

## APPENDIX

### Comparison of 3DVPAS to Sawyer–Eliassen Model

Many studies have solved a Sawyer–Eliassen (SE) equation in order to understand the balanced, linear response of a vortex to imposed heat and/or momentum forcings. An alternative methodology is to use the linear vortex model 3DVPAS, first described by Nolan and Grasso (2003) and most extensively in Hodys and Nolan (2007) and Nolan et al. (2007). Aside from the fact that 3DVPAS can also be used to calculate the response to asymmetric forcings and to diagnose three-dimensional unstable modes, the most relevant differences between using 3DVPAS and SE for calculating the symmetric response to symmetric forcing is that 3DVPAS is time dependent and nonhydrostatic, whereas SE is steady state and balanced. Nevertheless, when a steady forcing is imposed in 3DVPAS, the time-dependent solution generally converges to a result that is very similar to that of SE. While this near equivalence of solutions has been known for some time and was stated in Rozoff et al. (2012), it has not previously been demonstrated

---

<sup>13</sup> Indeed, several studies that have examined the effect of friction in isolation found vortex spindown rather than intensification (Eliassen and Lystad 1977; Montgomery et al. 2001; Menelaou et al. 2014).

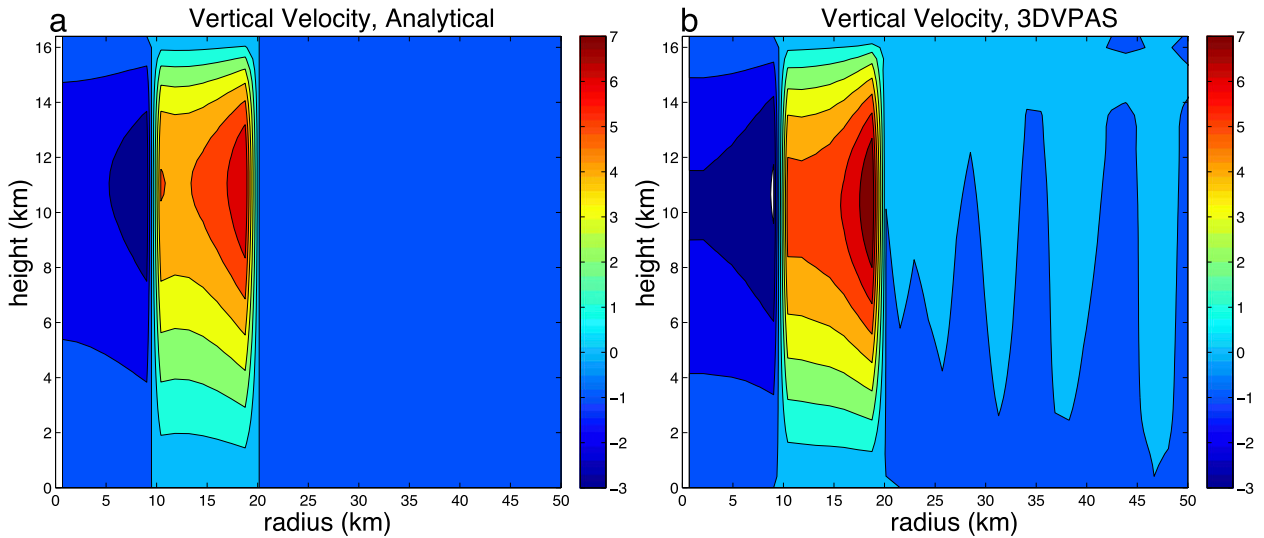


FIG. A1. Vertical velocity for the (a) analytical solution and (b) 3DVPAS numerical solution for the response to heating of the S07 vortex (see text for details). Contour interval is  $1 \text{ m s}^{-1}$ . Note that the vertical velocity in (a) is actually log-pressure vertical velocity, whereas the geometric vertical velocity is shown in (b). However, both (a) and (b) use geometric height as the vertical coordinate for plotting.

explicitly. Here, we demonstrate that 3DVPAS yields a nearly identical result to the analytical solutions of SE given in S07 and Rozoff et al. (2008).

S07 derived the SE secondary circulation equation for an inviscid vortex in thermal wind balance on an  $f$  plane, with log-pressure height as the vertical coordinate. This second-order PDE [their (8)] is given by

$$\frac{\partial}{\partial r} \left[ A \frac{\partial(r\psi)}{r\partial r} + B \frac{\partial\psi}{\partial z} \right] + \frac{\partial}{\partial z} \left[ B \frac{\partial(r\psi)}{r\partial r} + C \frac{\partial\psi}{\partial z} \right] = \frac{g}{c_p T_0} \frac{\partial Q}{\partial r}, \quad (\text{A1})$$

where  $\psi$  is the radial–vertical streamfunction,  $g$  is the gravitational acceleration,  $c_p$  is the specific heat capacity at constant pressure,  $T_0$  is a constant reference temperature,  $Q$  is the diabatic heating, and  $A$ ,  $B$ , and  $C$  are the static stability, baroclinicity, and inertial stability, respectively [see (5)–(7) of S07 for their definitions]. The log-pressure height (which qualitatively resembles geometric height) is given by  $z = H \log(p_0/p)$ , where  $H$  is a constant scale height and  $p_0$  is a constant reference pressure. For realistic spatial distributions of the coefficients  $A$ ,  $B$ , and  $C$ , (A1) can only be solved numerically. By considering a barotropic vortex ( $B = 0$ ) with constant static stability and piecewise-constant inertial stability, as well as assuming that  $Q$  and  $\psi$  are separable in radius and height, S07 were able to solve (A1) analytically for  $\psi$  and, therefore, for the vertical velocity  $w$ . The solution for  $w$  is given by (24) of S07. In Fig. A1a, we plot

the analytical solution given in S07 for  $w$  (which is log-pressure vertical velocity) for their vortex A as a function of radius and geometric height.<sup>A1</sup> Vortex A [whose analytical form is given by (11)–(13) and Table 1 of S07] is a Rankine vortex with maximum winds of  $70 \text{ m s}^{-1}$  and an RMW of 20 km. The heating is constant with radius in an annulus from  $r = 10$  to 20 km and is zero everywhere else. As a result, there is upward motion where there is heating, and downward motion both inward and outward of the annulus.

In 3DVPAS, we use the analytical vortex profile given in S07 as the basic state, and the heating profile given in S07 as the constant forcing for a 24-h integration, which is sufficient time for a steady state to be achieved. Note that all variables in 3DVPAS are defined on a discrete, staggered grid, the vertical coordinate is geometric height, and there is numerical diffusion (set in this case to  $40 \text{ m}^2 \text{ s}^{-1}$ ).<sup>A2</sup> In spite of these differences, the distribution and magnitude of  $w$  (which is geometric vertical velocity) in 3DVPAS (Fig. A1b) is nearly identical to that of the analytical solution (Fig. A1a). This is further evident in Fig. A2, which shows the radial profile of  $w$  at

<sup>A1</sup> We calculate the analytical solution at discrete grid points corresponding to the 3DVPAS grid. This allows us to plot log-pressure vertical velocity as a function of geometric height so that we can best compare the analytical solution to 3DVPAS.

<sup>A2</sup> Note that the calculations in section 4 used a diffusivity of  $10 \text{ m}^2 \text{ s}^{-1}$  and also differ in grid spacing from that in the appendix.

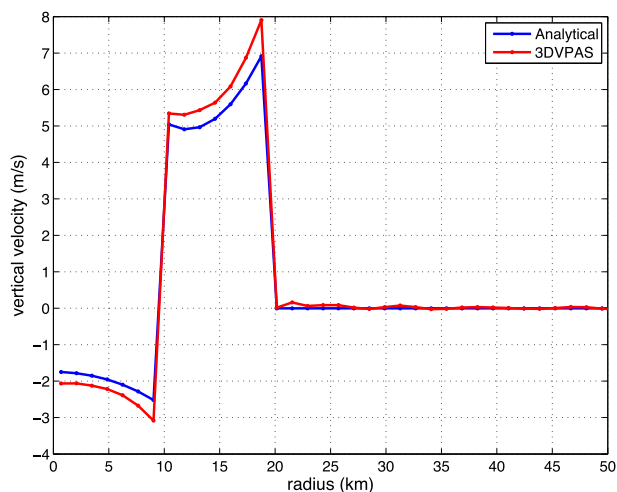


FIG. A2. Vertical velocity vs radius for the height where the maximum  $w$  occurs. Note that this height is slightly different between the analytical (11.1 km) and 3DVPAS (10.7 km) solutions.

the height of its maximum. It is clear that 3DVPAS is essentially equivalent in result to the SE model for the problem of the symmetric response of a vortex to symmetric forcing.

#### REFERENCES

- Abarca, S. F., and M. T. Montgomery, 2013: Essential dynamics of secondary eyewall formation. *J. Atmos. Sci.*, **70**, 3216–3230, doi:10.1175/JAS-D-12-0318.1.
- , and —, 2014: Departures from axisymmetric balance dynamics during secondary eyewall formation. *J. Atmos. Sci.*, **71**, 3723–3738, doi:10.1175/JAS-D-14-0018.1.
- Black, M. L., J. F. Gamache, F. D. Marks Jr., C. E. Samsury, and H. E. Willoughby, 2002: Eastern Pacific hurricanes Jimena of 1991 and Olivia of 1994: The effect of vertical shear on structure and intensity. *Mon. Wea. Rev.*, **130**, 2291–2312, doi:10.1175/1520-0493(2002)130<2291:EPHJOA>2.0.CO;2.
- Bryan, G. H., 2012: Effects of surface exchange coefficients and turbulence length scales on the intensity and structure of numerically simulated hurricanes. *Mon. Wea. Rev.*, **140**, 1125–1143, doi:10.1175/MWR-D-11-00231.1.
- , and R. Rotunno, 2009: The maximum intensity of tropical cyclones in axisymmetric numerical model simulations. *Mon. Wea. Rev.*, **137**, 1770–1789, doi:10.1175/2008MWR2709.1.
- Bui, H. H., R. K. Smith, M. T. Montgomery, and J. Peng, 2009: Balanced and unbalanced aspects of tropical cyclone intensification. *Quart. J. Roy. Meteor. Soc.*, **135**, 1715–1731, doi:10.1002/qj.502.
- Chen, H., D.-L. Zhang, J. Carton, and R. Atlas, 2011: On the rapid intensification of hurricane Wilma (2005). Part I: Model prediction and structural changes. *Wea. Forecasting*, **26**, 885–901, doi:10.1175/WAF-D-11-00001.1.
- Dunion, J. P., 2011: Rewriting the climatology of the tropical North Atlantic and Caribbean Sea atmosphere. *J. Climate*, **24**, 893–908, doi:10.1175/2010JCLI3496.1.
- Eliassen, A., 1951: Slow thermally or frictionally controlled meridional circulation in a circular vortex. *Astrophys. Norv.*, **5**, 19–60.
- , and M. Lystad, 1977: The Ekman layer of a circular vortex. A numerical and theoretical study. *Geophys. Norv.*, **31**, 1–16.
- Emanuel, K. A., 1995: The behavior of a simple hurricane model using a convective scheme based on subcloud-layer entropy equilibrium. *J. Atmos. Sci.*, **52**, 3960–3968, doi:10.1175/1520-0469(1995)052<3960:TBOASH>2.0.CO;2.
- , 2012: Self-stratification of tropical cyclone outflow. Part II: Implications for storm intensification. *J. Atmos. Sci.*, **69**, 988–996, doi:10.1175/JAS-D-11-0177.1.
- Evans, C., and R. E. Hart, 2008: Analysis of the wind field evolution associated with the extratropical transition of Bonnie (1998). *Mon. Wea. Rev.*, **136**, 2047–2065, doi:10.1175/2007MWR2051.1.
- Hill, K. A., and G. M. Lackmann, 2009: Analysis of idealized tropical cyclone simulations using the Weather Research and Forecasting Model: Sensitivity to turbulence parameterization and grid spacing. *Mon. Wea. Rev.*, **137**, 745–765, doi:10.1175/2008MWR2220.1.
- Hodys, D., and D. S. Nolan, 2007: Linear anelastic equations for atmospheric vortices. *J. Atmos. Sci.*, **64**, 2947–2959, doi:10.1175/JAS3991.1.
- Hogsett, W. A., and S. R. Stewart, 2014: Dynamics of tropical cyclone intensification: Deep convective cyclonic “left movers.” *J. Atmos. Sci.*, **71**, 226–242, doi:10.1175/JAS-D-12-0284.1.
- Holland, G. J., 1997: The maximum potential intensity of tropical cyclones. *J. Atmos. Sci.*, **54**, 2519–2541, doi:10.1175/1520-0469(1997)054<2519:TMPIOT>2.0.CO;2.
- , and R. T. Merrill, 1984: On the dynamics of tropical cyclone structural changes. *Quart. J. Roy. Meteor. Soc.*, **110**, 723–745, doi:10.1002/qj.49711046510.
- Houze, R. A., Jr., 2010: Clouds in tropical cyclones. *Mon. Wea. Rev.*, **138**, 293–344, doi:10.1175/2009MWR2989.1.
- Jorgensen, D. P., 1984b: Mesoscale and convective-scale characteristics of mature hurricanes. Part II: Inner core structure of Hurricane Allen (1980). *J. Atmos. Sci.*, **41**, 1287–1311, doi:10.1175/1520-0469(1984)041<1287:MACSCO>2.0.CO;2.
- Judt, F., and S. S. Chen, 2013: Reply to “Comments on ‘Convectively generated potential vorticity in rainbands and formation of the secondary eyewall in Hurricane Rita of 2005.’” *J. Atmos. Sci.*, **70**, 989–992, doi:10.1175/JAS-D-12-0151.1.
- Keptert, J. D., 2013: How does the boundary layer contribute to eyewall replacement cycles in axisymmetric tropical cyclones. *J. Atmos. Sci.*, **70**, 2808–2830, doi:10.1175/JAS-D-13-046.1.
- , and Y. Wang, 2001: The dynamics of boundary layer jets within the tropical cyclone core. Part II: Nonlinear enhancement. *J. Atmos. Sci.*, **58**, 2485–2501, doi:10.1175/1520-0469(2001)058<2485:TDOBLJ>2.0.CO;2.
- , and D. S. Nolan, 2014: Reply to “Comments on ‘How does the boundary layer contribute to eyewall replacement cycles in axisymmetric tropical cyclones?’” *J. Atmos. Sci.*, **71**, 4692–4704, doi:10.1175/JAS-D-14-0014.1.
- Kieu, C. Q., 2012: An investigation into the contraction of the hurricane radius of maximum wind. *Meteor. Atmos. Phys.*, **115**, 47–56, doi:10.1007/s00703-011-0171-7.
- Kimball, S. K., and M. S. Mulekar, 2004: A 15-year climatology of North Atlantic tropical cyclones. Part I: Size parameters. *J. Climate*, **17**, 3555–3575, doi:10.1175/1520-0442(2004)017<3555:AYCONA>2.0.CO;2.
- , and F. C. Dougherty, 2006: The sensitivity of idealized hurricane structure and development to the distribution of vertical levels in MM5. *Mon. Wea. Rev.*, **134**, 1987–2008, doi:10.1175/MWR3171.1.
- Kossin, J. P., J. A. Knaff, H. I. Berger, D. C. Herndon, T. A. Cram, C. S. Velden, R. J. Murnane, and J. D. Hawkins, 2007:

- Estimating hurricane wind structure in the absence of aircraft reconnaissance. *Wea. Forecasting*, **22**, 89–101, doi:[10.1175/WAF985.1](https://doi.org/10.1175/WAF985.1).
- Menelaou, K., M. K. Yau, and Y. Martinez, 2014: Some aspects of the problem of secondary eyewall formation in idealized three-dimensional nonlinear simulations. *J. Adv. Model. Earth Syst.*, **6**, 491–512, doi:[10.1002/2014MS000316](https://doi.org/10.1002/2014MS000316).
- Montgomery, M. T., H. D. Snell, and Z. Yang, 2001: Axisymmetric spindown dynamics of hurricane-like vortices. *J. Atmos. Sci.*, **58**, 421–435, doi:[10.1175/1520-0469\(2001\)058<0421:ASDOHL>2.0.CO;2](https://doi.org/10.1175/1520-0469(2001)058<0421:ASDOHL>2.0.CO;2).
- Mrowiec, A. A., S. T. Garner, and O. M. Pauluis, 2011: Axisymmetric hurricane in a dry atmosphere: Theoretical framework and numerical experiments. *J. Atmos. Sci.*, **68**, 1607–1619, doi:[10.1175/2011JAS3639.1](https://doi.org/10.1175/2011JAS3639.1).
- Nolan, D. S., and M. T. Montgomery, 2002: Nonhydrostatic, three-dimensional perturbations to balanced, hurricane-like vortices. Part I: Linearized formulation, stability, and evolution. *J. Atmos. Sci.*, **59**, 2989–3020, doi:[10.1175/1520-0469\(2002\)059<2989:NTDPTB>2.0.CO;2](https://doi.org/10.1175/1520-0469(2002)059<2989:NTDPTB>2.0.CO;2).
- , and L. D. Grasso, 2003: Nonhydrostatic, three-dimensional perturbations to balanced, hurricane-like vortices. Part II: Symmetric response and nonlinear simulations. *J. Atmos. Sci.*, **60**, 2717–2745, doi:[10.1175/1520-0469\(2003\)060<2717:NTPTBH>2.0.CO;2](https://doi.org/10.1175/1520-0469(2003)060<2717:NTPTBH>2.0.CO;2).
- , Y. Moon, and D. P. Stern, 2007: Tropical cyclone intensification from asymmetric convection: Energetics and efficiency. *J. Atmos. Sci.*, **64**, 3377–3405, doi:[10.1175/JAS3988.1](https://doi.org/10.1175/JAS3988.1).
- Pu, Z., X. Li, and E. J. Zipser, 2009: Diagnosis of the initial and forecast errors in the numerical simulation of the rapid intensification of Hurricane Emily (2005). *Wea. Forecasting*, **24**, 1236–1251, doi:[10.1175/2009WAF2222195.1](https://doi.org/10.1175/2009WAF2222195.1).
- Rotunno, R., and G. H. Bryan, 2012: Effects of parameterized diffusion on simulated hurricanes. *J. Atmos. Sci.*, **69**, 2284–2299, doi:[10.1175/JAS-D-11-0204.1](https://doi.org/10.1175/JAS-D-11-0204.1).
- Rozoff, C. M., W. H. Schubert, and J. P. Kossin, 2008: Some dynamical aspects of tropical cyclone concentric eyewalls. *Quart. J. Roy. Meteor. Soc.*, **134**, 583–593, doi:[10.1002/qj.237](https://doi.org/10.1002/qj.237).
- , D. S. Nolan, J. P. Kossin, F. Zhang, and J. Fang, 2012: The roles of an expanding wind field and inertial stability in tropical cyclone secondary eyewall formation. *J. Atmos. Sci.*, **69**, 2621–2643, doi:[10.1175/JAS-D-11-0326.1](https://doi.org/10.1175/JAS-D-11-0326.1).
- Schubert, W. H., and J. J. Hack, 1982: Inertial stability and tropical cyclone development. *J. Atmos. Sci.*, **39**, 1687–1697, doi:[10.1175/1520-0469\(1982\)039<1687:ISATCD>2.0.CO;2](https://doi.org/10.1175/1520-0469(1982)039<1687:ISATCD>2.0.CO;2).
- , and B. D. McNoldy, 2010: Application of the concepts of Rossby length and Rossby depth to tropical cyclone dynamics. *J. Adv. Model. Earth Syst.*, **2**, 7, doi:[10.3894/JAMES.2010.2.7](https://doi.org/10.3894/JAMES.2010.2.7).
- , C. M. Rozoff, J. L. Vigh, B. D. McNoldy, and J. P. Kossin, 2007: On the distribution of subsidence in the hurricane eye. *Quart. J. Roy. Meteor. Soc.*, **133**, 595–605, doi:[10.1002/qj.49](https://doi.org/10.1002/qj.49).
- Schwendike, J., and J. D. Kepert, 2008: The boundary layer winds in Hurricanes Danielle (1998) and Isabel (2003). *Mon. Wea. Rev.*, **136**, 3168–3192, doi:[10.1175/2007MWR2296.1](https://doi.org/10.1175/2007MWR2296.1).
- Shapiro, L. J., and H. E. Willoughby, 1982: The response of balanced hurricanes to local sources of heat and momentum. *J. Atmos. Sci.*, **39**, 378–394, doi:[10.1175/1520-0469\(1982\)039<0378:TROBHT>2.0.CO;2](https://doi.org/10.1175/1520-0469(1982)039<0378:TROBHT>2.0.CO;2).
- Smith, R. K., 1981: The cyclostrophic adjustment of vortices with application to tropical cyclone modification. *J. Atmos. Sci.*, **38**, 2021–2030, doi:[10.1175/1520-0469\(1981\)038<2021:TCAOVW>2.0.CO;2](https://doi.org/10.1175/1520-0469(1981)038<2021:TCAOVW>2.0.CO;2).
- , M. T. Montgomery, and N. V. Sang, 2009: Tropical cyclone spin-up revisited. *Quart. J. Roy. Meteor. Soc.*, **135**, 1321–1335, doi:[10.1002/qj.428](https://doi.org/10.1002/qj.428).
- Stern, D. P., and D. S. Nolan, 2009: Reexamining the vertical structure of tangential winds in tropical cyclones: Observations and theory. *J. Atmos. Sci.*, **66**, 3579–3600, doi:[10.1175/2009JAS2916.1](https://doi.org/10.1175/2009JAS2916.1).
- , and —, 2011: On the vertical decay rate of the maximum tangential winds in tropical cyclones. *J. Atmos. Sci.*, **68**, 2073–2094, doi:[10.1175/2011JAS3682.1](https://doi.org/10.1175/2011JAS3682.1).
- , J. R. Brisbois, and D. S. Nolan, 2014: An expanded dataset of hurricane eyewall sizes and slopes. *J. Atmos. Sci.*, **71**, 2747–2762, doi:[10.1175/JAS-D-13-0302.1](https://doi.org/10.1175/JAS-D-13-0302.1).
- Van Sang, N., R. K. Smith, and M. T. Montgomery, 2008: Tropical cyclone intensification and predictability in three dimensions. *Quart. J. Roy. Meteor. Soc.*, **134**, 563–582, doi:[10.1002/qj.235](https://doi.org/10.1002/qj.235).
- Vigh, J. L., 2010: Formation of the hurricane eye. Ph.D. dissertation, Colorado State University, 538 pp. [Available online at [http://www.ral.ucar.edu/staff/jvigh/documents/vigh2010\\_dissertation\\_corrected\\_color\\_hyperlinks.pdf](http://www.ral.ucar.edu/staff/jvigh/documents/vigh2010_dissertation_corrected_color_hyperlinks.pdf).]
- , J. A. Knaff, and W. H. Schubert, 2012: A climatology of hurricane eye formation. *Mon. Wea. Rev.*, **140**, 1405–1426, doi:[10.1175/MWR-D-11-00108.1](https://doi.org/10.1175/MWR-D-11-00108.1).
- Wang, Y., 2008: Structure and formation of an annular hurricane simulated in a fully compressible, nonhydrostatic model—TCM4. *J. Atmos. Sci.*, **65**, 1505–1527, doi:[10.1175/2007JAS2528.1](https://doi.org/10.1175/2007JAS2528.1).
- Weng, Y., and F. Zhang, 2012: Assimilating airborne Doppler radar observations with an ensemble Kalman filter for convection-permitting hurricane initialization and prediction: Katrina (2005). *Mon. Wea. Rev.*, **140**, 841–859, doi:[10.1175/2011MWR3602.1](https://doi.org/10.1175/2011MWR3602.1).
- Willoughby, H. E., 1990: Temporal changes in the primary circulation of tropical cyclones. *J. Atmos. Sci.*, **47**, 242–264, doi:[10.1175/1520-0469\(1990\)047<0242:TCOTPC>2.0.CO;2](https://doi.org/10.1175/1520-0469(1990)047<0242:TCOTPC>2.0.CO;2).
- , and M. E. Rahn, 2004: Parametric representation of the primary hurricane vortex. Part I: Observations and evaluation of the Holland (1980) model. *Mon. Wea. Rev.*, **132**, 3033–3048, doi:[10.1175/MWR2831.1](https://doi.org/10.1175/MWR2831.1).
- , J. A. Clos, and M. G. Shoreibah, 1982: Concentric eye walls, secondary wind maxima, and the evolution of the hurricane vortex. *J. Atmos. Sci.*, **39**, 395–411, doi:[10.1175/1520-0469\(1982\)039<0395:CEWSWM>2.0.CO;2](https://doi.org/10.1175/1520-0469(1982)039<0395:CEWSWM>2.0.CO;2).
- , H.-L. Jin, S. J. Lord, and J. M. Piotrowicz, 1984: Hurricane structure and evolution as simulated by an axisymmetric, nonhydrostatic numerical model. *J. Atmos. Sci.*, **41**, 1169–1186, doi:[10.1175/1520-0469\(1984\)041<1169:HSAEAS>2.0.CO;2](https://doi.org/10.1175/1520-0469(1984)041<1169:HSAEAS>2.0.CO;2).
- Zhang, J. A., R. F. Rogers, D. S. Nolan, and F. D. Marks Jr., 2011: On the characteristic height scales of the hurricane boundary layer. *Mon. Wea. Rev.*, **139**, 2523–2535, doi:[10.1175/MWR-D-10-05017.1](https://doi.org/10.1175/MWR-D-10-05017.1).